J|A|C|S
ARTICLES
Published on Web 03/06/2004

Quantum Mechanical/Molecular Mechanical Investigation of the Mechanism of C−H Hydroxylation of Camphor by Cytochrome P450$_{cam}$: Theory Supports a Two-State Rebound Mechanism

Jan C. Schöneboom,[†] Shimrit Cohen,[‡] Hai Lin,[†] Sason Shaik,*[,‡] and Walter Thiel*[,†]

Contribution from the Max-Planck-Institut für Kohlenforschung, Kaiser-Wilhelm-Platz 1, D-45470 Mülheim an der Ruhr, Germany, and the Department of Organic Chemistry and the Lise Meitner Center for Computational Quantum Chemistry, The Hebrew University, 91904 Jerusalem, Israel

Received November 28, 2003; E-mail: (W.T.) thiel@mpi-muelheim.mpg.de; (S.S.) sason@yfaat.ch.huji.ac.il

Abstract: The stereospecific cytochrome P450-catalyzed hydroxylation of the $C^5-H^{(5-exo)}$ bond in camphor has been studied theoretically by a combined quantum mechanical/molecular mechanical (QM/MM) approach. Density functional theory is employed to treat the electronic structure of the active site (40−100 atoms), while the protein and solvent environment (ca. 24 000 atoms) is described by the CHARMM force field. The calculated energy profile of the hydrogen-abstraction oxygen-rebound mechanism indicates that the reaction takes place in two spin states (doublet and quartet), as has been suggested earlier on the basis of calculations on simpler models ("two-state reactivity"). While the reaction on the doublet potential energy surface is nonsynchronous, yet effectively concerted, the quartet pathway is truly stepwise, including formation of a distinct intermediate substrate radical and a hydroxo−iron complex. Comparative calculations in the gas phase demonstrate the effect of the protein environment on the geometry and relative stability of intermediates (in terms of spin states and redox electromers) through steric constraints and electronic polarization.

I. Introduction

Cytochrome P450 enzymes are hemoproteins that catalyze hydroxylation of nonactivated C−H bonds with a potentially high degree of stereo- and regioselectivity.[1] For example, the bacterial enzyme P450$_{cam}$ hydroxylates camphor at the C^5 position and produces exclusively the *exo*-alcohol (see Scheme 1).[2]

The identity of the active oxidant is generally assumed to be compound I[3] (**2** in Scheme 2), an oxoiron(IV) porphyrin radical cation. While the intermediacy of its precursor in P450$_{cam}$-mediated hydroxylation, hydroperoxy complex **1**, has recently been ascertained by electron nuclear double resonance (ENDOR) spectroscopy under turnover conditions,[4] compound I remains elusive and the mechanism of hydroxylation is still controversial.

In the consensus rebound mechanism[5] (see Scheme 3), compound I (**2**) initially abstracts a hydrogen from the substrate,

Scheme 1

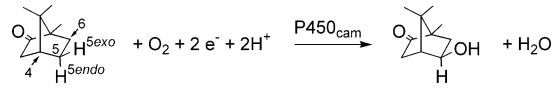

Scheme 2

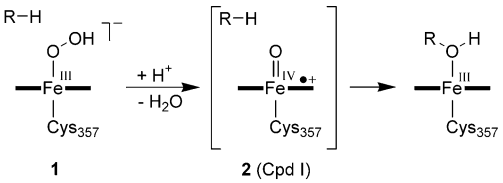

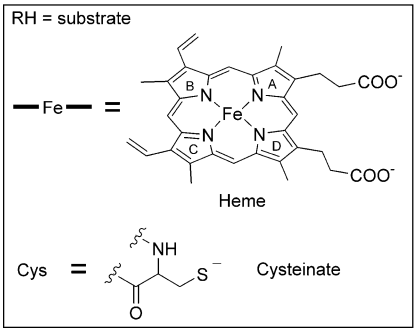

followed by rebound of the intermediate radical onto the iron-bound hydroxyl (**3**) to furnish the ferric alcohol complex **4**. The rebound mechanism has gained support through the years from

* To whom correspondence should be addressed: (W.T.) phone +49-208-306-2150, fax +49-208-306-2996; (S.S.) phone +972-2-6585909, fax +972-2-6584680.
[†] Max-Planck-Institut für Kohlenforschung.
[‡] The Hebrew University.

(1) Ortiz de Montellano, P. R., Ed. *Cytochrome P450: Structure, Mechanisms and Biochemistry*, 2nd ed.; Plenum Press: New York, 1995; Vol. 2.
(2) Mueller, E. J.; Lioda, P. J.; Sligar, S. G. In *Cytochrome P450: Structure, Mechanisms and Biochemistry*, 2nd ed.; Ortiz de Montellano, P. R., Ed.; Plenum Press: New York, 1995; Vol. 2., Chapt. 3.
(3) Groves, J. T.; Watanabe, Y. *J. Am. Chem. Soc.* **1988**, *110*, 8443.
(4) Davydov, R.; Makris, T. M.; Kofman, V.; Werst, D. E.; Sligar, S. G.; Hoffman, B. M. *J. Am. Chem. Soc.* **2001**, *123*, 1403.
(5) Groves, J. T.; McClusky, G. A. *J. Am. Chem. Soc.* **1976**, *98*, 859.

Scheme 3

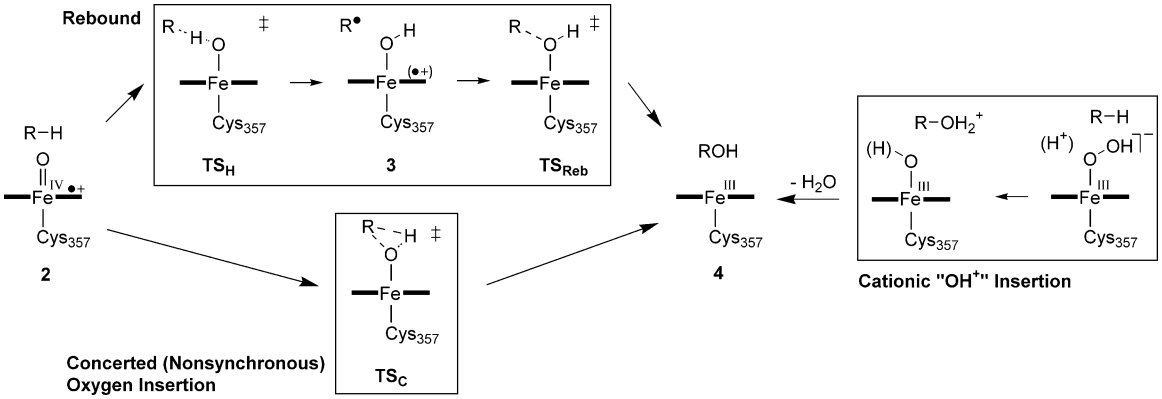

experimental observations such as, e.g., observed stereochemical scrambling[6] and intrinsic kinetic isotope effect measurements.[7] Stereochemical scrambling has also been observed in $P450_{cam}$, which can remove either an *exo*- or an *endo*-hydrogen from the C^5 position of camphor but apparently permits rebound solely from the exo face (producing exclusively 5-*exo*-hydroxycamphor).[6,8]

The controversy regarding the mechanistic details of C−H hydroxylation by P450 mainly arose from radical-clock experiments,[9] which yield lifetimes of the substrate radicals that are much too short to correspond to true intermediates. To explain the seemingly contradictory experimental findings, alternative hypotheses and extensions to the original rebound mechanism have been put forward: (i) A concerted, nonsynchronous oxygen insertion pathway was suggested with compound I **(2)** being the active oxidant[10] (see Scheme 3). The intermediate radicals are components of a reacting ensemble (or transition structure) with lifetimes on the order of femtoseconds. The reaction is assumed to proceed through a bifurcated transition state where one reaction channel leads directly to the formation of the hydroxylated product and the other, minor pathway leads into a radical manifold, but not an intermediate, with subsequent rearrangement. (ii) A two-state reactivity (TSR) mechanism was proposed[11] on the basis of theoretical arguments, which combines features of both the stepwise rebound and the concerted oxygen insertion mechanism. This scenario invokes two spin states, the doublet and the quartet state. The reaction involves hydrogen abstraction on both spin surfaces via similar transition states (**TS_H**, see Scheme 3). The transformation on the doublet surface then proceeds by a barrierless recombination to give the product alcohol complex **4** and thus is effectively concerted. In contrast, the quartet pathway—as proposed in the original rebound mechanism—involves a significant barrier for rebound and a genuine transition state, **TS_{Reb}**, and thus represents a truly stepwise reaction that gives rise to a discrete radical intermediate **3**. (iii) It has also been postulated that a second oxidant other than compound I is present in the catalytic cycle of P450 enzymes, which catalyzes the hydroxylation reaction. Specifically, small amounts of products that apparently originate in rearrangement of a cationic intermediate are observed, which leads to the suggestion that the second oxidant performs hydroxylation by inserting "OH^+" into the C−H bond of the substrate. A species that has been linked to such cationic hydroxylating activity is the iron hydroperoxy complex **1**.[9,12] Experimental evidence, however, makes this third (cationic hydroxylation) scenario less convincing than a scenario involving compound I only. Thus, recent ^{1}H ENDOR studies[4] are consistent with hydroxylation mediated by compound I but seem to exclude the iron hydroperoxy complex as the active species. Similar conclusions may be drawn from a study of the Thr252Ala mutant of $P450_{cam}$, in which the formation of compound I is suppressed.[13] It was shown that the mutant enzyme catalyzes the epoxidation of camphene, albeit with a much smaller efficiency than the wild-type enzyme. However, the mutant enzyme exhibited no activity for camphor hydroxylation. This indicates that, in the absence of compound I, the iron hydroperoxy species could act as an epoxidizing agent but not as a C−H hydroxylating one. We shall therefore consider only the hydroxylation mechanism induced by compound I.

Theoretical studies have made significant contributions to the mechanistic discussion by complementing experimental observations with calculations on unresolved aspects of the catalytic cycle of cytochrome P450.[14] Thus, density functional theory (DFT) calculations on different gas-phase model compounds have dealt with all the above-mentioned scenarios in some detail. At present, the conclusions from theory are consistent with the TSR scenario for P450-mediated hydroxylation,[11,15,16] while no low-energy pathway has been found so far for concerted oxygen insertion[15d,17,18] or a cationic hydroxylation mechanism involving

(6) Gelb, M. H.; Heimbrook, D. C.; Malkonen, P.; Sligar, S. G. *Biochemistry* **1982**, *21*, 370.
(7) Hjelmeland, L. M.; Aronow, L.; Trudell, J. *Biochem. Biophys. Res. Commun.* **1976**, *76*, 541.
(8) Atkins, W. M.; Sligar, S. G. *J. Am. Chem. Soc.* **1987**, *109*, 3754.
(9) Newcomb, M.; Toy, P. H. *Acc. Chem. Res.* **2000**, *33*, 449.
(10) Newcomb, M.; Le Tadic-Biadatti, M.-H.; Chestney, D. L.; Roberts, E. S.; Hollenberg, P. F. *J. Am. Chem. Soc.* **1995**, *117*, 12085.
(11) (a) Shaik, S.; Filatov, M.; Schröder, D.; Schwarz, H. *Chem. Eur. J.* **1998**, *4*, 193. (b) Ogliaro, F.; Harris, N.; Cohen, S.; Filatov, M.; de Visser, S. P.; Shaik, S. *J. Am. Chem. Soc.* **2000**, *122*, 8977. (c) Harris, N.; Cohen, S.; Filatov, M.; Ogliaro, F.; Shaik, S. *Angew. Chem., Int. Ed.* **2000**, *39*, 2003. (d) Schröder, D.; Shaik, S.; Schwarz, H. *Acc. Chem. Res.* **2000**, *33*, 139. (e) Ogliaro, F.; de Visser, S. P.; Groves, J. T.; Shaik, S. *Angew. Chem., Int. Ed.* **2001**, *40*, 2874. (f) Shaik, S.; de Visser, S. P.; Ogliaro, F.; Schwarz, H.; Schröder, D. *Curr. Opin. Chem. Biol.* **2002**, *6*, 556. (g) Kumar, D.; de Visser, S. P.; Shaik, S. *J. Am. Chem. Soc.* **2003**, *125*, 13024.
(12) (a) Toy, P. H.; Dhanabalasingam, B.; Newcomb, M.; Hanna, I. H.; Hollenberg, P. F. *J. Org. Chem.* **1997**, *62*, 9114. (b) Toy, P. H.; Newcomb, M.; Hollenberg, P. F. *J. Am. Chem. Soc.* **1998**, *120*, 7719. (c) Toy, P. H.; Newcomb, M.; Coon, M. J.; Vaz, A. D. N. *J. Am. Chem. Soc.* **1998**, *120*, 9718. (d) Newcomb, M.; Hollenberg, P. F.; Coon, M. J. *Arch. Biochem. Biophys.* **2003**, *409*, 72.
(13) Jin, S.; Makris, T. M.; Bryson, T. A.; Sligar, S. G.; Dawson, J. H. *J. Am. Chem. Soc.* **2003**, *125*, 3406.
(14) (a) Loew, G. H.; Harris, D. L. *Chem. Rev.* **2000**, *100*, 407. (b) Harris, D. L. *Curr. Opin. Chem. Biol.* **2001**, *5*, 724. (c) Harris, D. L.; Loew, G. H. *J. Porphyrins Phthalocyanines* **2001**, *5*, 334. (d) Harris, D. L. *J. Inorg. Biochem.* **2002**, *91*, 568. (e) Park, J.-Y.; Harris, D. L. *J. Med. Chem.* **2003**, *46*, 1645.

the ferric hydroperoxy complex.[19−21] In a recent study,[15f] Kamachi and Yoshizawa investigated a gas-phase model including full camphor and a methylthiolate ligated iron−porphyrin. However, while such studies provide insight into the intrinsic reactivity of a given model, they cannot account for the specific steric and electrostatic interactions within the protein pocket. For example, in $P450_{cam}$, the substrate camphor is positionally restrained by a hydrogen bond from Tyr96 to its carbonyl oxygen and by hydrophobic interactions with Val295 and Val396. Moreover, hydrogen bonding to the proximal cysteinate sulfur has a remarkable influence on the computed electronic structure of compound I[22] and the activity of P450 as a whole.[23] It was demonstrated by model calculations that such effects may have a large impact, inter alia, on computed relative activation barriers for the low- and high-spin components of TSR.[24] To test the TSR hypothesis, *a study is therefore required that realistically accounts for effects of the protein environment*. Currently, the state-of-the-art method for this purpose is the combined quantum mechanics−molecular mechanics (QM/MM) approach.[25] We have previously presented a QM/MM study on compound I of cytochrome $P450_{cam}$,[22] which highlighted the advantages of this combined method to model the reactive species in the specific enzyme environment. A recent QM/MM study on P450 camphor hydroxylation[26] considered only the H-abstraction step and only the quartet spin state. In the present paper, we report combined QM/MM calculations on camphor hydroxylation in the specific enzyme environment, as well as pure QM calculations on the isolated QM subsystems in the gas phase. Our study addresses both possible oxygenation pathways that start from compound I, i.e., the concerted oxygen insertion and the rebound mechanism (H-abstraction plus radical recombination), and presents the complete energy profiles for both the doublet and the quartet spin surfaces. Our results indicate that the hydrogen-abstraction oxygen-rebound pathway in two spin states (TSR scenario) is operational in $P450_{cam}$-mediated C−H hydroxylation. The comparison to analogous calculations on the isolated QM system in the gas phase allows us to interpret factors that are considered to be relevant to the role of the protein environment in enzyme catalysis. The paper is organized as follows. Details of our computational model are given in section II. The results of our computations can be found in section III. The mechanistic implications of our calculations are discussed in section IV, while section V contains concluding remarks.

II. Computational Details

A. Setup of the System. To prepare suitable initial structures for the QM/MM calculations, we started from a X-ray structure tentatively assigned to compound I[27] and built a complete model of the solvated enzyme by adding missing hydrogen atoms and solvent water. The entire system consists of 24 394 atoms, including 16 956 atoms in the solvent. This initial system was then relaxed by performing pure force-field energy minimizations and molecular dynamics (MD) simulations, with the CHARMM force field[28] as implemented in the CHARMM program,[29] during which the coordinates of the heme and the coordinating Cys357 were kept fixed. Details of these force-field calculations are given in ref 22.

B. Snapshots. We have separately investigated two snapshots (after 29 and 40 ps of equilibration) from an MD trajectory obtained in the preparatory force-field calculations by means of QM/MM geometry optimizations. We started from the optimized snapshot geometries; the potential energy surfaces (PES) were scanned along suitable coordinates (see below) to generate continuous reaction paths, and the lowest and highest points on these paths were then fully optimized to locate the minima and transition states, respectively. The results from these two independent studies (snapshots 29 and 40) are fully consistent, with variations in relative energies of less than 7%. This strongly suggests that the optimized conformations are representative for the reactive pathways studied. Furthermore, we have optimized selected structures for two more snapshots (snapshot 40man and snapshot 50)[22] where we have generated initial structures by replacing the coordinates of the heme, Cys357, and camphor from the MD run by the corresponding coordinates of stationary points optimized for snapshot 40; subsequently, these systems were fully reoptimized. Since all results are qualitatively very similar, we shall focus here on snapshot 40 and present only key data for snapshot 29. The complete data are given in the Supporting Information.

C. QM/MM Calculations. The general QM/MM methodology adopted in the present study is documented extensively in refs 22 and 30. In the following, we only describe the aspects relevant to the present work.

1. QM Methods. The QM part was treated with unrestricted Kohn−Sham (UKS) DFT with the B3LYP density functional.[31] Higher lying electromers of a given spin state (see below, e.g, for **3**-Fe^{IV}) were calculated by altering the orbital occupations of the UKS determinants manually and converging the SCF equations to the corresponding

(15) (a) Yoshizawa, K.; Kagawa, Y.; Shiota, Y. *J. Phys. Chem. B* **2000**, *104*, 12365. (b) Yoshizawa, K.; Ohta, T.; Eda, M.; Yamabe, T. *Bull. Chem. Soc. Jpn.* **2000**, *73*, 401. (c) Yoshizawa, K.; Shiota, Y.; Kagawa, Y. *Bull. Chem. Soc. Jpn.* **2000**, *73*, 2669. (d) Yoshizawa, K.; Kamachi, T.; Shiota, Y. *J. Am. Chem. Soc.* **2001**, *123*, 9806. (e) Yoshizawa, K. *Coord. Chem. Rev.* **2002**, *226*, 251. (f) Kamachi, T.; Yoshizawa, K. *J. Am. Chem. Soc.* **2003**, *125*, 4652. (g) Kamachi, T.; Yoshizawa, K. *J. Inorg. Biochem.* **2003**, *96*, 161.

(16) Hata, M.; Hirano, Y.; Hoshino, T.; Tsuda, M. *J. Am. Chem. Soc.* **2001**, *123*, 6410.

(17) Schröder, D.; Fiedler, A.; Hrusak, J.; Schwarz, H. *J. Am. Chem. Soc.* **1992**, *114*, 1215.

(18) (a) Filatov, M.; Shaik, S. *J. Phys. Chem. A* **1998**, *102*, 3835. (b) de Visser, S. P.; Ogliaro, F.; Shaik, S. *Chem. Commun.* **2001**, 2322. (c) Filatov, M.; Reckien, W.; Peyerimhoff, S. D.; Shaik, S. *J. Phys. Chem. A* **2000**, *104*, 12014.

(19) Ogliaro, F.; de Visser, S. P.; Cohen, S.; Sharma, P. K.; Shaik, S. *J. Am. Chem. Soc.* **2002**, *124*, 2806.

(20) Sharma, P. K.; de Visser, S. P.; Shaik, S. *J. Am. Chem. Soc.* **2003**, *125*, 8698.

(21) Kamachi, T.; Shiota, Y.; Ohta, T.; Yoshizawa, K. *Bull. Chem. Soc. Jpn.* **2003**, *76*, 721.

(22) Schöneboom, J. C.; Lin, H.; Reuter, N.; Thiel, W.; Cohen, S.; Ogliaro, F.; Shaik, S. *J. Am. Chem. Soc.* **2002**, *124*, 8142.

(23) Yoshioka, S.; Tosha, T.; Takahashi, S.; Ishimori, K.; Hori, H.; Morishima, I. *J. Am. Chem. Soc.* **2002**, *124*, 14571.

(24) de Visser, S. P.; Ogliaro, F.; Sharma, P. K.; Shaik, S. *Angew. Chem., Int. Ed.* **2002**, *41*, 1947.

(25) (a) Warshel, A.; Levitt, M. *J. Mol. Biol.* **1976**, *103*, 227. (b) Field, M. J.; Bash, P. A.; Karplus, M. *J. Comput. Chem.* **1990**, *11*, 700. (c) Gao, J. In *Reviews in Computational Chemistry*; Lipkowitz, K. B.; Boyd, D. B., Eds.; VCH Publishers: New York, 1996; Vol. 7, p 119. (d) Mordasini, T. Z.; Thiel, W. *Chimia* **1998**, *58*, 288. (e) Monard, G.; Merz, K. M., Jr. *Acc. Chem. Res.* **1999**, *32*, 904.

(26) Guallar, V.; Baik, M. H.; Lippard, S. J.; Friesner, R. A. *Proc. Natl. Acad. Sci. U.S.A.* **2003**, *100*, 6998.

(27) Schlichting, I.; Berendzen, J.; Chu, K.; Stock, A. M.; Maves, S. A.; Benson, D. E.; Sweet, R. M.; Ringe, D.; Petsko, G. A.; Sligar, S. G. *Science* **2000**, *287*, 1615.

(28) CHARMM22 force field: MacKerell, A. D., Jr.; Bashford, D.; Bellott, M.; Dunbrack, R. L., Jr.; Evanseck, J. D.; Field, M. J.; Fischer, S.; Gao, J.; Guo, H.; Ha, S.; Joseph-McCarthy, D.; Kuchnir, L.; Kuczera, K.; Lau, F. T. K.; Mattos, C.; Michnick, S.; Ngo, T.; Nguyen, D. T.; Prodhom, B.; Reiher, W. E., III; Roux, B.; Schlenkrich, M.; Smith, J. C.; Stote, R.; Straub, J.; Watanabe, M.; Wiorkiewicz-Kuczera, J.; Yin, D.; Karplus, M. *J. Phys. Chem. B* **1998**, *102*, 3586.

(29) Brooks, B. R.; Burccoleri, R. E.; Olafson, B. D.; States D. J.; Karplus, M. *J. Comput. Chem.* **1983**, *4*, 187.

(30) Sherwood, P.; de Vries, A. H.; Guest, M. F.; Schreckenbach, G.; Catlow, C. R. A.; French, S. A.; Sokol, A. A.; Bromley, S. T.; Thiel, W.; Turner, A. J.; Billeter, S.; Terstegen, F.; Thiel, S.; Kendrick, J.; Rogers, S. C.; Casci, J.; Watson, M.; King, F.; Karlsen, E.; Sjovoll, M.; Fahmi, A.; Schäfer, A.; Lennartz, C. *J. Mol. Struct. (THEOCHEM)* **2003**, *632*, 1.

(31) (a) Becke, A. D. *Phys. Rev. A* **1988**, *38*, 3098. (b) Lee, C.; Yang, W.; Parr, R. G. *Phys. Rev. B* **1988**, *37*, 85. (c) Becke, A. D. *J. Chem. Phys.* **1993**, *98*, 5648.

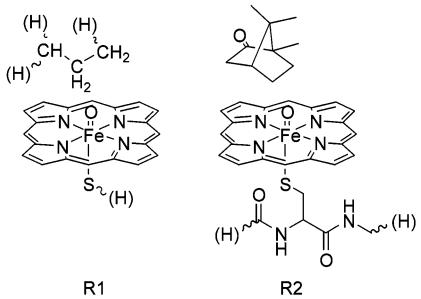

Figure 1. Definition of QM regions R1 and R2.

solution. For a given orbital occupation with three unpaired electrons, we considered only the lowest UKS determinant for the doublet state in each case.[11b] Two different QM regions, denoted R1 and R2, were employed (see Figure 1), which comprised the following sets of atoms: (i) R1 (51 QM atoms): Iron−oxo−porphyrin (without side chains of the heme), sulfur of Cys357, C^4H, C^5H_2, and C^6H_2 of camphor. In the gas-phase calculations, this corresponds to [FeO(SH)(porph)] + propane. (ii) R2 (84 QM atoms): Iron−oxo−porphyrin (without side chains of the heme), Cys357, CO group of Leu346, and NH−C^{α}H unit of Leu348, full camphor.

Additional single-point energy calculations were carried out for QM regions that are derived from R1 and R2 but extend onto the propionate side chains of the heme and the side chains of the neighboring amino acids that form salt bridges to the propionates. These QM regions are denoted R1-S*x* and R2-S*x* ($x = 1, 2, 3$) and will be further specified below. The basis sets used in the present investigations are abbreviated as B1 and B2. The iron atom is always described by a small-core effective core potential and the associated LACVP basis of a double-ζ quality.[32] Basis B1 employs a 6-31G basis on all other atoms. Basis B2 is augmented with a set of polarization and diffuse functions (6−31^+G*) on the six atoms coordinated to iron, the C^5 atom (6−31^+G*), and also on the $H^{(5-exo)}$ hydrogen atom (6−31^{++}G**) of camphor.[33] In the following, the QM level employed in a particular QM/MM calculation will be denoted by the expression QM region/basis set, e.g. R1/B1 or R2/B2.

2. QM/MM Methods. An electronic embedding scheme[34] was applied, i.e., the fixed MM charges were included into the one-electron Hamiltonian of the QM calculation and the QM/MM electrostatic interactions were evaluated from the QM electrostatic potential and the MM atomic charges. No cutoffs were introduced for the nonbonding MM and QM/MM interactions. To treat the QM/MM boundary, we used hydrogen link atoms with the charge shift model.[35,36]

3. Codes. For the QM treatment in the QM/MM as well as in the pure QM calculations, we employed the TURBOMOLE program.[37] All QM/MM calculations were performed with the ChemShell package.[30,38] The CHARMM22 force field[28,39] run through the DL-POLY program[40] was used for the treatment of the MM part of the system.

4. Gas-Phase Calculations. To assess the influence of the protein environment on the QM subsystem, gas-phase QM calculations were performed employing QM region R1 and basis B1 (i) as single-point energy calculations at the geometry of the system in the enzyme environment and (ii) as full geometry optimizations of the isolated species in the gas phase. The former will be referred to as $S_{p,g}$ (the system at the protein geometry in the gas phase) and the latter as $S_{g,g}$ (the gas-phase system optimized in the gas phase). Additional gas-phase optimizations were carried out for the hydrogen-abstraction step, by use of a QM model that includes full camphor as substrate, the oxo−iron(IV) porphyrin, and HS^- as the sixth ligand to iron.

5. Geometry Optimizations. The QM/MM optimizations included the following set of residues close to the active site: Pro86, Phe87, Tyr96, Pro100, Thr101, Leu244, Gly248, Asp251, Thr252, Val295, Asp297, Arg299, Phe350, His355, Leu356, Cys357, Leu358, Gly359, Gln360, Ile395, Val396, heme, camphor, Wat61, Wat253, and Wat325. This corresponds to a total of 442 optimized atoms from QM region R2 and the residues next to it. Geometry optimizations were performed with the HDLC optimizer,[41] which is part of ChemShell. A rational function optimizer with the Powell update (P-RFO) for an explicit Hessian[41] was used in transition-state optimizations. The nature of the transition states as first-order saddle points (one mode with an imaginary frequency) was confirmed by numerical calculation of the finite-difference Hessian for the set of QM atoms. The computationally demanding PES scans and frequency calculations were performed with the smaller QM region R1 and basis set B1. The stationary points optimized at this level of theory were then reoptimized in the enzyme environment with the larger QM region R2 and basis B2.

6. TDDFT. To confirm the stability of the UKS determinants used to describe the ground state, we have carried out time-dependent density functional theory (TDDFT) calculations both for the system in the enzyme environment and for the isolated gas-phase species, with QM region R1 and basis set B1. The TDDFT calculations in the enzyme environment are based on geometries and densities optimized at the QM/MM (R1/B1) level. The corresponding excitations for the isolated species are calculated at the gas-phase optimized geometries. These calculations were carried out with the ESCF module[42] of TURBOMOLE.

7. QM Calibration Study. To probe the intrinsic accuracy of the DFT approach in describing the H-abstraction barrier, we have carried out a calibration study employing different density functionals and basis sets. To this end, we have chosen the simplified molecular model $[FeO(SH)(NH_3)_4]^+ + CH_4$ (**5**) for this reaction (see section IIIB). The geometries of the model reactive complex **5** and the corresponding transition state for hydrogen abstraction **5-TS$_H$** were optimized with TURBOMOLE[37] using the B3LYP density functional[31] and the SV(P) basis.[43] A frequency calculation confirmed that the transition state has only one eigenmode with an imaginary frequency. Single-point calculations were done with the popular pure GGA functionals BP86[31a,44] and BLYP.[31a,b] As hybrid density functionals, in addition to B3LYP, we also tested the B97 (20% exact exchange, like B3LYP),[45] and PBE0 (25% exact exchange)[46] functionals. These DFT calculations were carried out with MOLPRO.[47] Additional basis sets employed for the single-point energy calculations were the SV, SVP, and TZVP sets taken from the TURBOMOLE library;[43,48] the cc-pVDZ and cc-pVQZ basis sets by Dunning et al.;[49] and a Wachters all-electron basis set for

(32) Hay, J. P.; Wadt, W. R. *J. Chem. Phys.* **1985**, *82*, 299.
(33) (a) Ditchfield, R.; Hehre, W. J.; Pople, J. A. *J. Chem. Phys.* **1971**, *54*, 724. (b) Hehre, W. J.; Ditchfield, R.; Pople, J. A. *J. Chem. Phys.* **1972**, *56*, 2257. (c) Hariharan, P. C.; Pople, J. A. *Theor. Chim. Acta* **1973**, *28*, 213. (d) Clark, T.; Chandrasekhar, J.; Spitznagel, G. W.; Schleyer, P. v. R. *J. Comput. Chem.* **1983**, *4*, 294.
(34) Bakowies, D.; Thiel, W. *J. Phys. Chem.* **1996**, *100*, 10580.
(35) Antes, I.; Thiel, W. *Hybrid Quantum Mechanical and Molecular Mechanical Methods*; Gao, J., Ed.; ACS Symposium Series 712; American Chemical Society; Washington, DC, 1998; pp 50−65.
(36) de Vries, A. H.; Sherwood, P.; Collins, S. J.; Rigby, A. M.; Rigutto, M.; Kramer, G. J. *J. Phys. Chem. B* **1999**, *103*, 6133.
(37) (a) Ahlrichs, R.; Bär, M.; Häser, M.; Horn, H.; Kölmel, C. *Chem. Phys. Lett.* **1989**, *162*, 165. (b) Ahlrichs, R.; Bär, M.; Baron, H.-P.; Bauernschmitt, R.; Böcker, S.; Ehrig, M.; Eichkorn, K.; Elliot, S.; Furche, F.; Häser, M.; Horn, H.; Hättig, C.; Huber, C.; Huniar, U.; Kattanneck, M.; Köhn, A.; Kölmel, C.; Kollwitz, M.; May, K.; Ochsenfeld, C.; Öhm, H.; Schäfer, A.; Schneider, U.; Treutler, O.; v. Arnim, M.; Weigend, F.; Weis, P.; Weiss, H. TURBOMOLE 5.5, University of Karlsruhe, Germany, 2002.
(38) ChemShell is a modular QM/MM program developed in the European QUASI project under the coordination of P. Sherwood. See http://www.cse.clrc.ac.uk/qcg/chemshell.
(39) For details about the generation and geometric features of the snapshot structures, nonstandard force field parameters, and QM/MM geometry optimizations, see ref 22 and Supporting Information thereof.
(40) Smith, W.; Forester, T. *J. Mol. Graph.* **1996**, *14*, 136.
(41) Billeter, S. R.; Turner, A. J.; Thiel, W. *Phys. Chem. Chem. Phys.* **2000**, *2*, 2177.
(42) (a) Bauernschmitt, R.; Ahlrichs, R. *Chem. Phys. Lett.* **1996**, *256*, 454. (b) Bauernschmitt, R.; Ahlrichs, R. *J. Chem. Phys.* **1996**, *104*, 9047. (c) Ochsenfeld, C.; Gauss, J.; Ahlrichs, R.; *J. Chem. Phys.* **1995**, *103*, 7401.
(43) Schäfer, A.; Horn, H.; Ahlrichs, R. *J. Chem. Phys.* **1992**, *97*, 2571.
(44) Perdew, J. P. *Phys. Rev. B* **1986**, *33*, 8822.
(45) Becke, A. D. *J. Chem. Phys.* **1997**, *107*, 8554.
(46) Adamo, C.; Barone, V. *J. Chem. Phys.* **1999**, *110*, 6158.

iron with an additional diffuse d function and a set of f polarization functions in the contraction [8s7p4d1f].[50]

III. Results

A. Concerted Oxygen Insertion Pathway. By use of the isolated QM system R1 in the gas phase with basis set B1, scans of the potential energy surface describing the concerted oxygen insertion pathway were performed in the doublet and quartet spin states. The scans were started from the product complex **4** and ended at the reactants **2** (compound I and camphor). Between these ends, we continuously varied the distances between the pairs of atoms C^5-H^5, $O-H^5$, C^5-O, and Fe−O and did partial optimizations with constraints on the corresponding internal coordinates. Small steps were used in regions near the maxima. The resulting energy profiles in the quartet and doublet states are shown in Figure S-1 of the Supporting Information, which also contains detailed numerical data regarding energies, bond lengths, angles, and spin densities along the scans.

The results from the PES scans indicate that the process has high barriers of approximately 50 and 60 kcal/mol for the doublet and quartet states, respectively. Moreover, when the number of geometry constraints was reduced, the structures along the path were found to be unstable and optimizations led to geometries not related to the reaction. Transition-state optimizations that were started from the maxima in the energy profiles did not locate suitable transition structures. Despite the limitations of the present procedure (e.g., incomplete scans of the PES), these finding strongly indicate that no low-energy pathway for the concerted oxygen-insertion pathway is viable. We note that previous gas-phase studies on simpler models reached the same conclusion.[17,18]

It seems quite unlikely that the presence of the protein environment can change the PES so dramatically that a low-energy path for concerted oxygen insertion would become accessible. Exploratory QM/MM constrained geometry optimizations (QM region R1, basis B1) in the region of highest energy from the gas-phase scan indeed yield relative energies above 45 kcal/mol also in the enzyme. We have therefore decided against performing more detailed QM/MM calculations for the concerted mechanism.

B. Rebound Mechanism. 1. Hydrogen Abstraction from Methane by Model Compound 5. Before presenting the results for camphor hydroxylation by compound I, we consider a simple test case in order to explore the intrinsic accuracy of the DFT method in describing the H-abstraction barrier, which corresponds to the rate-limiting step in the rebound mechanism. This study employed the simplified molecular model $[FeO(SH)(NH_3)_4]^+ + CH_4$, which is depicted in Figure 2.

This model system[51] includes all features essential for the hydrogen abstraction step, i.e., the oxoferryl moiety, the thiolate ligand, and the octahedral coordination geometry of the iron center with four nitrogen donors. The electronic ground state of the cationic ferryl complex is a triplet ($S = 1$) with two unpaired electrons occupying d−p π^* orbitals, and is hence isoelectronic to the ferryl oxene moiety in compound I. Selected structural data from B3LYP/SV(P) optimizations of **5** and **5-TS$_H$** are shown in Figure 2.

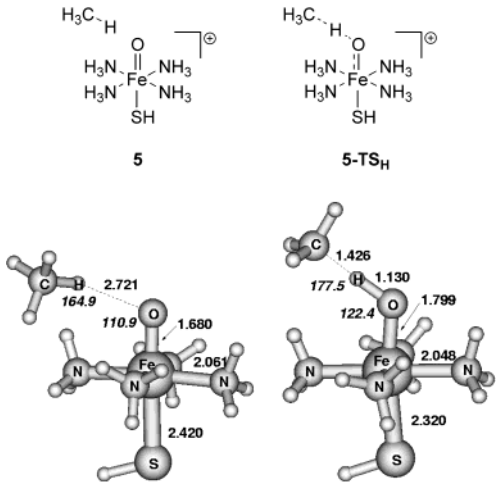

Figure 2. Simplified model for the H-abstraction step, $[FeO(SH)(NH_3)_4]^+ + CH_4$. Optimized geometries [B3LYP/SV(P)] of the reactive complex **5** and the transition state **5-TS$_H$** are shown. Distances are given in angstroms; angles (in italic type) are given in degrees.

Table 1. Activation Energies[a] for H-Abstraction in the Model System (see Figure 2) for Different Density Functionals and Basis Sets

Different Density Functionals, Basis AE1[b]					
BP86	BLYP	B3LYP	B97	PBE0	
22.4	25.2	19.5	20.1	15.1	
Different Basis Sets, B3LYP Density Functional					
B1	B2	SV	SVP	TZVP	AE2[c]
22.7	19.5	25.4	21.7	21.4	19.3

[a] Activation energies are given in kilocalories per mole. [b] AE1: Fe Wachters all electron [8s7p4d1f], other atoms cc-pVTZ (508 basis functions). [c] AE2: Fe Wachters [8s7p4d1f], other atoms cc-pVQZ without g functions (892 basis functions).

After the full geometry optimizations at the B3LYP/SV(P) level, single-point calculations with different density functionals and basis sets were performed. The results are summarized in Table 1. We note that the B3LYP-calculated barriers with basis sets B1 and B2 are 22.7 and 19.5 kcal/mol, respectively. They are thus close to the barriers (see below) obtained for the larger iron porphyrin model systems (R1/B1, $S_{g,g} = 19.5$ kcal/mol for both ^{2}A and ^{4}A states). This underscores the fact that the chosen simple model is realistic.

Applying different density functionals with the same large basis set (AE1, 508 basis functions) yields activation energies ranging from 25.2 kcal/mol (BLYP) to 15.1 kcal/mol (PBE0). The pure GGA functionals BP86 and BLYP give the highest

(47) Amos, R. D.; Bernhardsson, A.; Berning, A.; Celani, P.; Cooper, D. L.; Deegan, M. J. O.; Dobbyn, A. J.; Eckert, F.; Hampel, C.; Hetzer, G.; Knowles, P. J.; Korona, T.; Lindh, R.; Lloyd, A. W.; McNicholas, S. J.; Manby, F. R.; Meyer, W.; Mura, M. E.; Nicklass, A.; Palmieri, P.; Pitzer, R.; Rauhut, G.; Schütz, M.; Schumann, U.; Stoll, H.; Stone, A. J.; Tarroni, R.; Thorsteinsson, T.; Werner, H.-J. MOLPRO, a package of ab initio programs designed by H.-J. Werner and P. J. Knowles, version 2002.1, 2002.
(48) Schäfer, A.; Huber, C.; Ahlrichs, R. *J. Chem. Phys.* **1994**, *100*, 5829.
(49) (a) Dunning, T. H., Jr. *J. Chem. Phys.* **1989**, *90*, 1007. (b) Woon, D. E.; Dunning, T. H., Jr. *J. Chem. Phys.* **1993**, *98*, 1358.
(50) (a) Wachters, A. J. H. *J. Chem. Phys.* **1970**, *52*, 1033. (b) Hay, P. J. *J. Chem. Phys.* **1977**, *66*, 4377. (c) Bauschlicher, C. W., Jr.; Langhoff, S. R.; Barnes, L. A. *J. Chem. Phys.* **1989**, *91*, 2399.
(51) A closely related nonheme Fe^{IV}=O complex has recently been characterized by X-ray crystallography: see Rohde, J.-U.; In, J.-H.; Lim, M. H.; Brennessel, W. W.; Bukowski, M. R.; Stubna, A.; Münck, E.; Nam, W.; Que, L., Jr. *Science* **2003**, *299*, 1037. This complex, $[Fe(O)(TMC)(NCCH_3)]^{2+}$ (TMC = 1,4,5,11-tetramethyl-1,4,8,11-tetraazacyclotetradecane), features an Fe−O bond length of 1.646(3) Å and four equatorial amino ligands with an average Fe−N bond distance of 2.091 Å, in close agreement with the optimized geometry calculated for **5**.

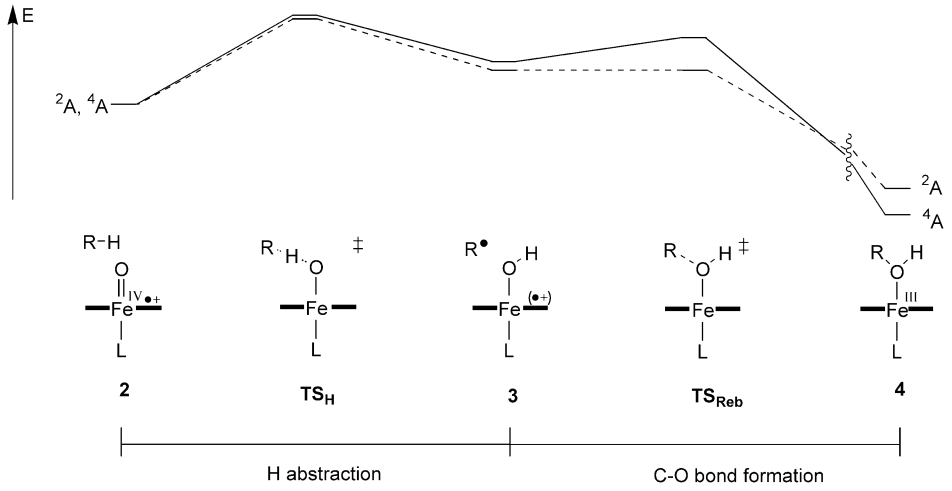

		2 (RC)	TS_H	3	TS_{Reb}	4
Snapshot 40	^{2}A	**0 (0)**	19.5 (21.1)	14.0 (9.4)	14.3	-37.8 (-47.1)
	^{4}A	-0.1 (0.01)	20.6 (21.8)	14.9 (10.5)	17.0	-42.7 (-49.8)
Snapshot 29	^{2}A	**0**	20.8	13.5	-	-37.9
	^{4}A	-0.1	21.6	14.6	17.4	-43.8
Gas phase	^{2}A	**0**	19.5	12.0	-	-50.2
	^{4}A	-0.02	19.5	12.5	16.2	-45.0

Figure 3. Computed energy profiles of the hydrogen-abstraction oxygen-rebound pathway. Relative energies (kilocalories per mole) from QM/MM optimizations of the full system (snapshot 40 and snapshot 29) and the isolated QM system in the gas phase are shown. The QM/MM results refer to R1/B1; the numbers in parentheses refer to R2/B2. The relative energies of **3** and $\mathbf{TS_{Reb}}$ always refer to the energetically lowest electromer (see discussion below).

barriers of 22.4 and 25.2 kcal/mol, respectively. The admixture of exact exchange apparently reduces the barrier. Hence, the B3LYP and B97 functionals, which both contain 20% exact exchange, predict barriers of 19.5 and 20.1 kcal/mol, respectively. The smallest barrier is obtained with the PBE0 functional, containing 25% exact exchange. The barriers calculated with the B3LYP density functional and different basis sets exhibit a clear trend: The simple double-ζ quality basis sets give the highest barriers (SV, 25.4 kcal/mol; B1, 22.7). The addition of polarization and/or diffuse functions reduces the relative energy by 3−4 kcal/mol (SVP, 21.7 kcal/mol; B2, 19.5 kcal/mol), whereas an increased flexibility in the valence region has only a minor effect (TZVP, 21.4 kcal/mol). The largest basis set AE2, which employs a Wachters basis for iron with additional f-polarization functions and a quadruple-ζ basis set with polarization up to f-functions on the other atoms (892 basis functions total), gives a barrier of 19.3 kcal/mol. One may thus conclude that basis B2, which is also used in the studies on the full system, provides essentially converged B3LYP results with respect to basis set size. On the other hand, the calculated barrier is very sensitive to the choice of the density functional; we observe variations of ca. 10 kcal/mol. Since there is no convincing reason to prefer one functional over the others,[52] this serves as a reminder that one may not expect quantitative accuracy from the calculated barriers for H-abstraction but should rather focus on qualitative comparisons.

We now turn to the rebound mechanism mediated by compound I of P450, using the QM/MM approach to model the entire enzyme and employing QM regions R1 and R2. For clarity, we will present the study of the mechanism in parts, dividing the entire process into (i) the H-abstraction phase (**2**, $\mathbf{TS_H}$), (ii) the properties of the intermediate iron hydroxo complex with the loosely coordinated substrate radical species (**3**), (iii) the rebound phase ($\mathbf{TS_{Reb}}$), and (iv) the product complex (**4**). The computed overall energy profile of the reaction is schematically depicted in Figure 3.

2. Hydrogen Abstraction from Camphor by Compound I (2). Starting from snapshot 40, the PES relevant to hydrogen abstraction was scanned at the R1/B1 level by constraining the internal coordinate corresponding to the distance $H^{(5-exo)}$—O at varying values and minimizing the remainder of the system. This was done separately on the doublet and quartet hypersurfaces. A plot of the QM/MM energies as a function of the constrained distance is shown in Figure S-2 of the Supporting Information. The relative QM/MM energies are dominated by the QM contributions, which reflect the chemical bond-breaking and bond-making process in the inner (QM) subsystem.

Stationary points were obtained from structures along the scan by releasing the $H^{(5-exo)}$—O bond constraint. These free geometry optimizations lead to a reactive complex (**2-RC**), the transition state for hydrogen abstraction ($\mathbf{TS_H}$), and the hydroxo iron complex with the loosely bound substrate radical (**3**). Comparison of the geometries separately optimized for the

(52) None of the calculated UKS determinants shows significant spin contamination, i.e., expectation values of the $\langle S^2 \rangle$ operator vary from 2.01 to 2.03 (triplet).

doublet and quartet states shows that the overall structures in the different spin states are in fact very similar and correspond to completely analogous conformations of the active-site environment, while small variations are observed for the atoms directly involved in the hydrogen transfer. The computed relative energies of **2** (RC) and $\mathbf{TS_H}$ are given in Figure 3. Selected geometry data from QM/MM optimizations of snapshot 40 and QM optimizations in the gas phase are shown in Figure 4. The spin densities, which serve as sensitive indicators of the electronic structure, are also given in Figure 4. Corresponding data for the other snapshot structures (QM/MM) are collected in the Supporting Information.

The transition states were calculated at the R1/B1 level to have a relative energy of (^{2}A/^{4}A) 19.5/20.6 kcal/mol with respect to the doublet (^{2}A) reactive complex **2**. The nature of the transition states as first-order saddle points was confirmed by numerical calculation of the Hessian and the vibrational frequencies of all QM atoms, which gave one mode with an imaginary frequency of (^{2}A/^{4}A) 811*i* cm^{-1}/561*i* cm^{-1}. The eigenmode corresponds to the expected motion of the hydrogen atom along the C−H−O axis. The calculations with the larger QM region R2 and basis B2 gave similar, albeit slightly higher, activation energies of (^{2}A/^{4}A) 21.1/21.8 kcal/mol. We also confirmed by additional minimizations starting from the transition structures that this saddle point truly connects the reactive complex (**2**) and the hydroxo intermediate (**3**). The activation energies computed for the isolated systems with QM region R1 and basis B1 in the gas phase are very similar to the corresponding QM/MM results: For the isolated species in the gas phase at the protein geometry ($S_{p,g}$), values of (^{2}A/^{4}A) 20.4/21.1 kcal/mol result. Optimizing the system in the gas phase ($S_{g,g}$) leads to activation energies of (^{2}A/^{4}A) 19.5/19.5 kcal/mol (see also Figure 3); hence the barriers are very close to the QM/MM results. Vibrational energies of the reactive complex **2** and the transition state $\mathbf{TS_H}$ were obtained from frequency calculations of the isolated species in the gas phase with QM region R1 and basis B1 for the ^{2}A as well as the ^{4}A state. These calculations predict that the zero-point energy (ZPE) decreases by 4.3 and 4.1 kcal/mol in the ^{2}A and ^{4}A states, respectively, when going from the reactive complex to the transition state. This loss of vibrational energy can be rationalized by the fact that the energy of the C−H vibration of the C^5−$H^{(5-exo)}$ bond in the reactant is missing in the transition state. Other changes, such as the breaking of the formally Fe=O double bond and the decreased rigidity of the heme (due to the Fe−O elongation and the distancing from the camphor), will also contribute to the ZPE difference. Inclusion of zero-point energy thus leads to barriers of (^{2}A/^{4}A) 15.2/15.4 kcal/mol for the gas-phase reaction. It is reasonable to assume that the effect is analogous in the enzyme environment, because it is mainly caused by the loss of the C−H vibrational energy within the substrate. One may estimate the ZPE energy difference between reactive complex and $\mathbf{TS_H}$ in the protein environment from the vibrational frequencies calculated for the QM atoms in the fixed matrix of protein atoms. This indeed leads to very similar ZPE energy differences of 4.9 and 4.5 kcal/mol (^{2}A and ^{4}A state). Because of positional constraints at the QM−MM border, the absolute ZPE is, however, much smaller in the protein environment as compared to the gas phase. Applying the gas-phase ZPE corrections to the QM/MM calculated activation energies yields estimates for the barriers of (^{2}A/^{4}A) 15.2/16.5 kcal/mol at the R1/B1 level and (^{2}A/^{4}A) 16.8/17.7 kcal/mol at the R2/B2 level.

In the transition structure the C^5−$H^{(5-exo)}$ distance is (^{2}A/^{4}A) 1.390/1.408 Å for R1/B1 and 1.359/1.369 Å for R2/B2, while the corresponding distances for O−$H^{(5-exo)}$ are 1.158/1.154 Å and 1.195/1.188 Å. In general, the transition state is closer to the product side, i.e., to the hydroxo intermediate **3**. Inspection of Figure 4 also shows a shift of unpaired spin density mainly from the oxygen atom to C^5 of camphor. The unpaired spin density on iron is also decreased, although to a lesser extent, while the porphyrin retains the π cation radical character. Hence, the system acquires some Fe^{III} character already in the transition state. (Note that the reactant **2** contains Fe^{IV} while the intermediate **3** may have either Fe^{IV} or Fe^{III}.) The reduction of spin density on iron and sulfur causes a concomitant shortening of the Fe−S bond length from (^{2}A/^{4}A) 2.573/2.552 Å in **2** to 2.533/2.523 Å in the transition state at the R2/B2 level. The $H^{(5-exo)}$ atom exhibits a small negative amount of spin density in all calculations, which is a typical feature of this system and consistent with previous model studies.[11,15,16]

A comparison of the electronic features obtained in the enzyme and gas phase calculations reveals a few subtle changes: (i) In the gas phase, there is significantly more spin density on the sulfur atom (as has already been discussed for compound I; see ref 22). For instance, the ratio of spin density porphyrin:sulfur in the ^{4}A reactive complex (gas phase) is 44:56, as compared to 80:20 in the QM/MM calculations. (ii) In the gas-phase transition state for hydrogen abstraction, the spin density distribution between iron and porphyrin is different in the doublet and quartet states: In the ^{2}A state, the spin density on iron (porphyrin) is 0.963 (−0.437). This species thus essentially retains the porphyrin π cation radical situation and therefore adopts some Fe^{III} character. In contrast, the ^{4}A transition state exhibits a spin density on iron (porphyrin) of 1.269 (0.123), which resembles more an Fe^{IV} state, with minor porphyrin π cation radical character. In the QM/MM calculations, both electronic states are of the Fe^{III} type. It seems, therefore, that the enzyme environment stabilizes the porphyrin π cation radical, and even though the barrier hardly changes, the protein in fact alters the transition-state species from $PorFe^{IV}$-like to ($Por^{\bullet+}Fe^{III}$)-like. Gas-phase calculations (basis B1) on the hydrogen abstraction step with camphor as a substrate show that the doublet transition state is energetically lower in the Fe^{IV}-type than in the Fe^{III}-type state by 1.5 kcal/mol (see Supporting Information). This further highlights the fact that the protein environment inverts the relative stability of the electromeric transition states.

3. Effect of the Propionate Side Chains. In the calculations with QM regions R1 and R2, the heme side chains and their environment were included in the MM calculation. Since the electrostatic force field terms are calculated from nonpolarizable atomic charges, these models cannot account for charge transfer involving these groups. To check the effect of the side chains, we have performed single-point energy calculations in the enzyme environment and in the gas phase, employing two larger QM regions that extend onto the propionate side chains of the heme. Including only the two propionate side chains on pyrrole rings A and D (see Scheme 2) into the previously discussed QM regions R1 and R2 leads to two new QM regions, denoted

Geometries

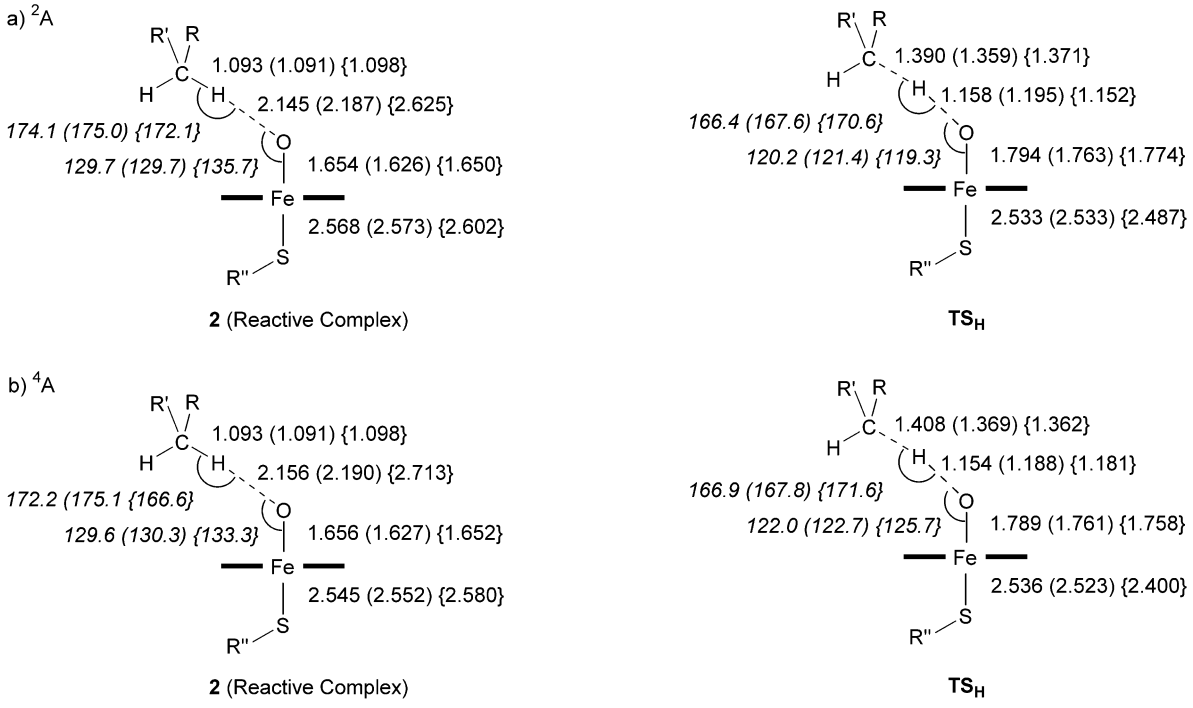

Spin densities

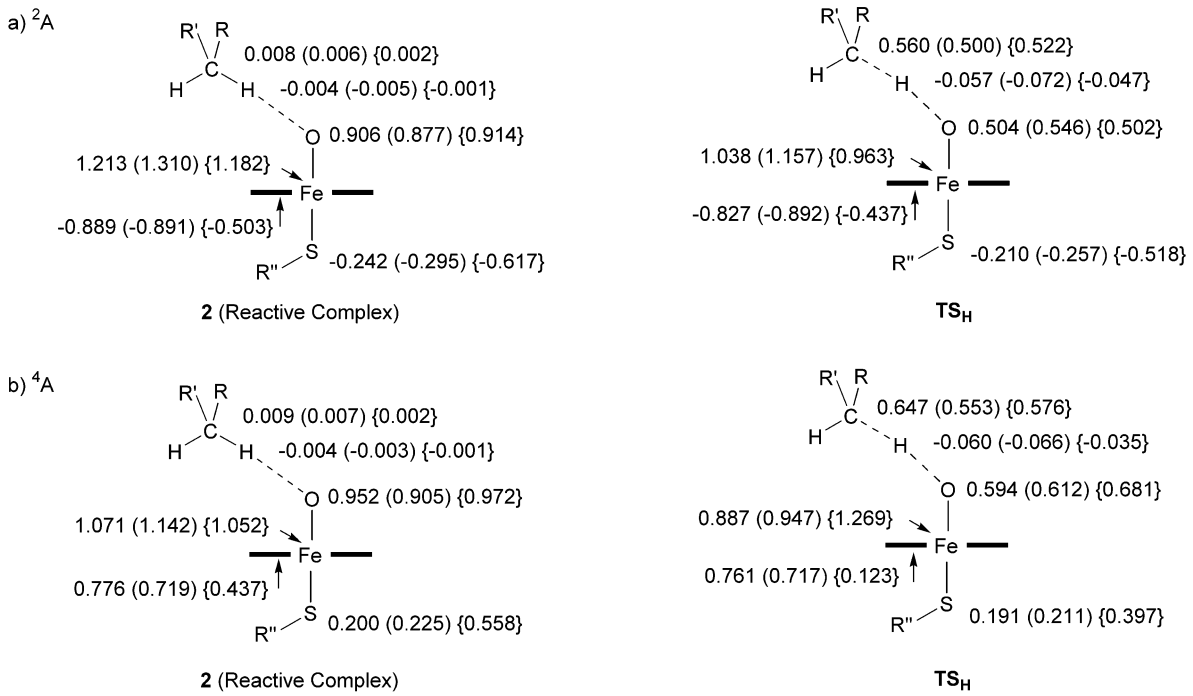

Figure 4. Selected structural data and spin densities for the reactive complex (**2**) and the transition state for H-abstraction (**TS_H**): (a) doublet state; (b) quartet state. The data refer to the following calculations: QM/MM optimization of snapshot 40, R1/B1 (QM/MM optimization of snapshot 40, R2/B2) {optimization of the isolated QM system in the gas phase, R1/B1}. Distances are given in angstroms; angles (in italic type) are given in degrees.

R1-S1 and R2-S1 (see Figure 5). The corresponding geometries were taken from QM/MM optimizations at the R1/B1 (R1-S1 single-point energy) or R2/B2 (R2-S2 single-point energy) level. Only the quartet spin state was considered.

The calculated activation energies and spin densities ρ for QM regions R1-S1 and R2-S1 are given in Figure 5. QM/MM single-point calculations in the protein environment yield barriers of 21.6 (R1-S1) and 24.2 (R2-S1) kcal/mol. The QM contribu-

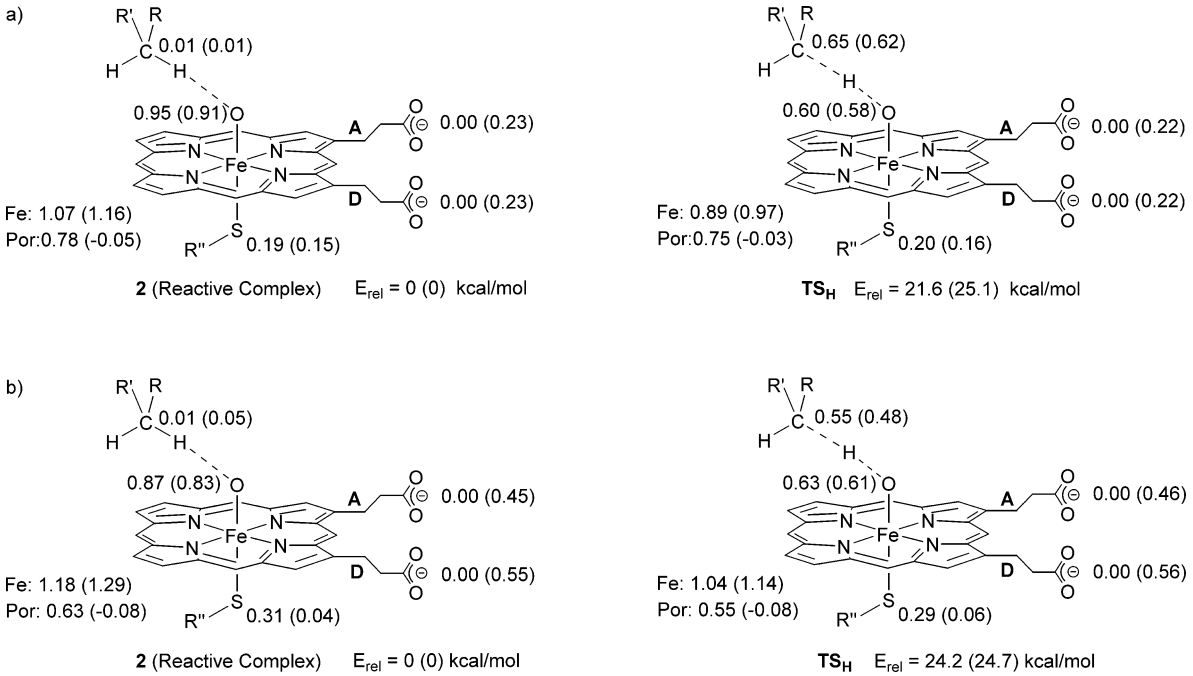

Figure 5. Effect of the heme propionate side chains (^{4}A state). (a) Single-point energy calculations at the R1-S1/B1 level, geometries optimized with R1/B1. (b) Single-point energy calculations at the R2-S1/B2 level, geometries optimized with R2/B2. Relative energies are given in kilocalories per mole; Mulliken unpaired (group) spin densities are given in units of the elementary charge, *e*. The labels refer to the following situations: QM/MM single-point calculation for snapshot 40 (QM single-point calculation of the isolated QM system in the gas phase). Por = sum of individual atomic spin densities of the atoms of the porphyrin macrocycle, without contributions from the propionate side chains.

tions to these values account for 20.5 (R1-S1) and 23.9 kcal/mol (R2-S1), respectively. Hence, the barriers are similar to those obtained with QM regions R1 and R2 (20.7 and 21.8 kcal/mol, respectively; see Figure 4). Mulliken analysis of the QM/MM calculated electron density shows no unpaired spin density on the carboxylate oxygens of the propionate side chains—neither in the reactive complex **2** nor in the transition state **TS$_H$**. Also, the Mulliken charges on these oxygen atoms are the same (sum of charges on all four oxygens for R1-S1, −2.81e), both in **2** and in **TS$_H$**. This demonstrates that there is no significant charge transfer between the propionate oxygens and the iron−porphyrin or the thiolate ligand, which justifies the use of QM regions R1 and R2 (excluding the propionate side chains). On the other hand, if the isolated QM system in the gas phase is considered, the calculated activation energies are 25.1 (R1-S1) and 24.8 (R2-S1) kcal/mol. The propionate oxygens now carry significant unpaired spin density (for R1-S1, **2**, 0.23e; **TS$_H$**, 0.22e) while the total charge density is reduced (sum of charges on all four oxygens for R1-S1, **2**, −1.93; **TS$_H$**, −1.94). The increased spin densities and decreased atomic charges show that localization of electronic charge on the carboxylate groups is unfavorable if there is no stabilization by a polarizing environment, as may have been expected.

To check whether the screening of the QM charge on the propionate oxygen atoms by the surrounding force-field atomic charges is described in a consistent manner, two further QM regions that are based on R1-S1 were considered: R1-S2 additionally includes the NHC(NH$_2$)$_2^+$ group of the neighboring Arg299, which forms a salt bridge with the A-propionate side chain, while R1-S3 incorporates the NHC(NH$_2$)$_2^+$ groups of both residues, Arg299 and Arg112, that form salt bridges with the A- and D-propionate side chains. QM/MM calculations with these QM regions were carried out on snapshot 29, for both the ^{2}A and the ^{4}A states (single-point calculations for R1-S2 and R1-S3 as well as geometry optimizations for R1-S2; R1-S2 data are given in the Supporting Information). The spin densities in the ^{4}A state are shown in Figure 6 for the most extended QM region: *it is apparent that the propionates, which are screened by the Arg residues, carry no spin density, neither in the enzyme nor in the gas phase*. The results from these and all other calculations with larger QM regions (R1-S*x*, *x* = 1, 2, 3), including those with geometry optimizations (R1-S2), invariably lead to the same conclusion: whenever the propionates are properly screened, be this in the gas phase or in the protein environment, there is no charge transfer from the propionates to the porphyrin or to the thiolate ligand.

4. Hydroxo Intermediate (3). The intermediate cluster **3** is characterized by four closely lying MOs, accommodating a total of five electrons (see Figure 7). As a consequence of this near-degeneracy of orbitals, there are several low-lying electronic states. Essentially, two electronic configurations, shown in Figure 7, are relevant to the representation of the ground state. In the first configuration, one of the three unpaired electrons is mainly localized on the iron center (and delocalized on the coordinating oxygen); the second one, in the mixed $a_{2u}/p\sigma$(S) orbital, is delocalized over the porphyrin and thiolate ligand; and the third one occupies the ϕ(C^5) orbital of the substrate radical. This electronic structure corresponds to an Fe^{III} species. As discussed previously,[53] a second electromer with low energy exists that has two unpaired electrons in the d_{xz} and d_{yz} orbitals of iron and the third one in ϕ(C^5). In this species, the formal oxidation state of iron is +IV and there is only residual unpaired spin density on porphyrin and sulfur ligands.

The Fe^{III} and Fe^{IV} electromers were optimized in the doublet and quartet spin states, respectively. The resulting relative

(53) Filatov, M.; Harris, N.; Shaik S. *Angew. Chem., Int. Ed.* **1999**, *38*, 3510.

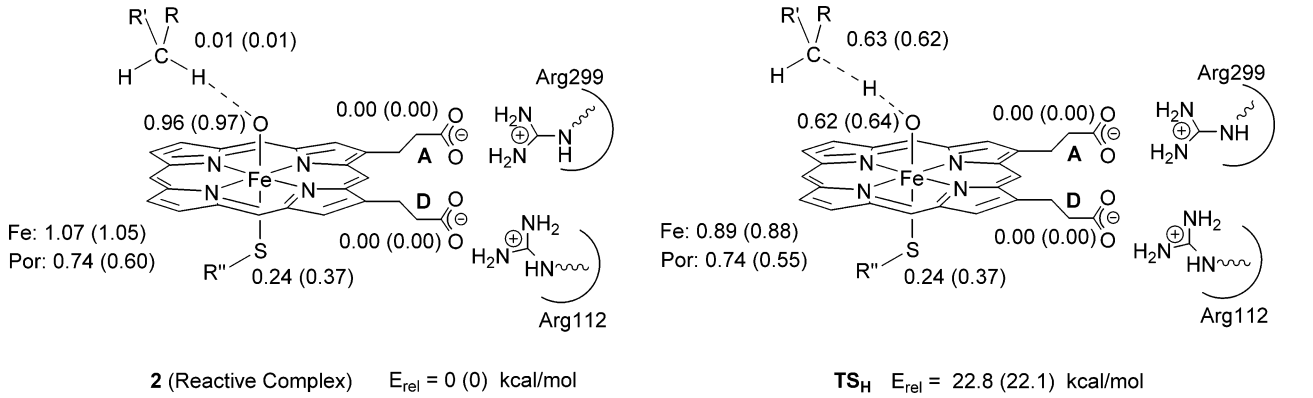

Figure 6. Effect of salt bridges. Single-point energy calculations at the R1-S3/B1 level, geometries optimized with R1/B1. Relative energies are given in kilocalories per mole, and Mulliken unpaired (group) spin densities are given in units of the elementary charge, *e*. The labels refer to the following situations: QM/MM single-point calculation for snapshot 29 (QM single-point calculation of the isolated QM system in the gas phase). Por = sum of individual atomic spin densities of the atoms of the porphyrin macrocycle, without contributions from the propionate side chains.

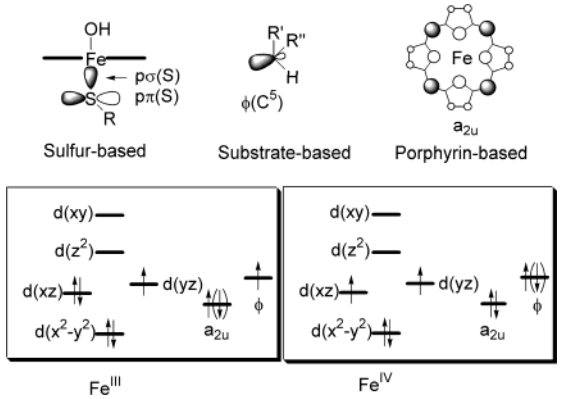

Figure 7. Hydroxo intermediate **3**: orbitals and occupations. The electron spin symbol in parentheses denotes the corresponding doublet configuration.

energies, relevant geometry data, and unpaired spin densities are summarized in Figure 8. The Fe^{III} and Fe^{IV} electromers are obviously close in energy. Generally, the doublet states are slightly preferred over the analogous quartet states. QM/MM calculations at the R1/B1 level predict an Fe^{III} ground state, with the Fe^{IV} state lying only ($^2A/^4A$) 1.12/1.10 kcal/mol higher in energy. When the larger QM region R2 is used, the gap is somewhat increased (2.55/2.20 kcal/mol). Interestingly, the ordering of the states is reversed in the optimized gas-phase species: here, the Fe^{IV} electromer is more stable than the Fe^{III} species by ($^2A/^4A$) 2.54/2.97 kcal/mol at the R1/B1 level. This stabilization of the Fe^{III} electromer in the enzyme environment is mainly due to the polarizing protein environment, while geometry relaxation in the gas phase has only a minor effect on the relative energies of the Fe^{III} vs Fe^{IV} state. These findings are in accord with DFT model calculations by Filatov et al.,[53] which demonstrated that a polarizing continuum environment stabilizes the Fe^{III} porphyrin radical ration state. This effect was attributed to the larger polarizability of the latter as compared to the Fe^{IV} species. The differences in the electronic structures of the Fe^{III} vs Fe^{IV} state are also manifest in the respective optimized structures. Most notably, the bond distances to the axial ligands are shorter in the Fe^{IV} electromer. This effect may be rationalized by the smaller Pauli repulsion of the electrons occupying the Fe-ligand σ bonds with the d_{xz}/d_{yz} electrons.[53] The dihedral angle $C^5-O-Fe-H$ determines the relative position of the C^5 atom with respect to the plane spanned by the atoms O−Fe−H. This parameter is important since it indicates from which position the carbon radical will attack the oxygen atom in the rebound phase. This dihedral angle is found to be negative, ranging from −10° to −28° in the QM/MM optimized structures. Hence, there is a clear preference for one conformation, indicating that attack in the rebound step will occur from one side of the O−Fe−H plane only. The unpaired spin densities summarized in Figure 8 conform to the electronic structures discussed above: The Fe^{III} (Fe^{IV}) species are typified by the spin density equivalent of approximately one (two) unpaired electron(s) on the iron center.

To qualitatively explore the nature of the lowest electronically excited states in each species, we used time-dependent DFT calculations for QM region R1 and basis B1. Details of these calculations are given in the Supporting Information. These calculations serve two purposes. First, they confirm that the considered configurations correspond to the electronic ground states of the discussed electromers. This is not a trivial issue, since in the present system, with high local symmetry and several possible occupations, the present approach might have converged to unstable solutions of the Kohn−Sham equations. Second, and more important, the calculations demonstrate that up to six electronic states exist below 1 eV, depending on electromer and spin state. This is due to the presence of nearly degenerate orbitals on both the ligands and the iron atom. The calculated excitation energies are not regarded as being quantitatively accurate, but they do indicate that several electronic states may be accessible at ambient conditions and contribute to the reactivity of the system. The consequences of such a multistate scenario have yet to be explored.

5. Rebound Step. In the second phase of the C−H hydroxylation mechanism—the rebound step—the substrate radical and the hydroxo complex **3** recombine to give the product alcohol complex **4**. Two internal coordinates are relevant to the PES of this process: the dihedral angle $\theta(C^5-Fe-O-H^{(5-exo)})$, describing the rotation of the OH group about the Fe−O axis, and the distance $r(C^5-O)$. We explored the PES of the rebound process first by straightforward scans along both internal coordinates separately and subsequently by calculating a two-dimensional grid at given values for $\theta(C^5-Fe-O-H^{(5-exo)})$ and $r(C^5-O)$, while relaxing all other degrees of freedom. Due to the computational effort, only the smaller QM region R1 and basis set B1 were employed. As discussed above, the intermediate cluster **3** exhibits four closely lying electronic states: these are

Geometries and relative energies

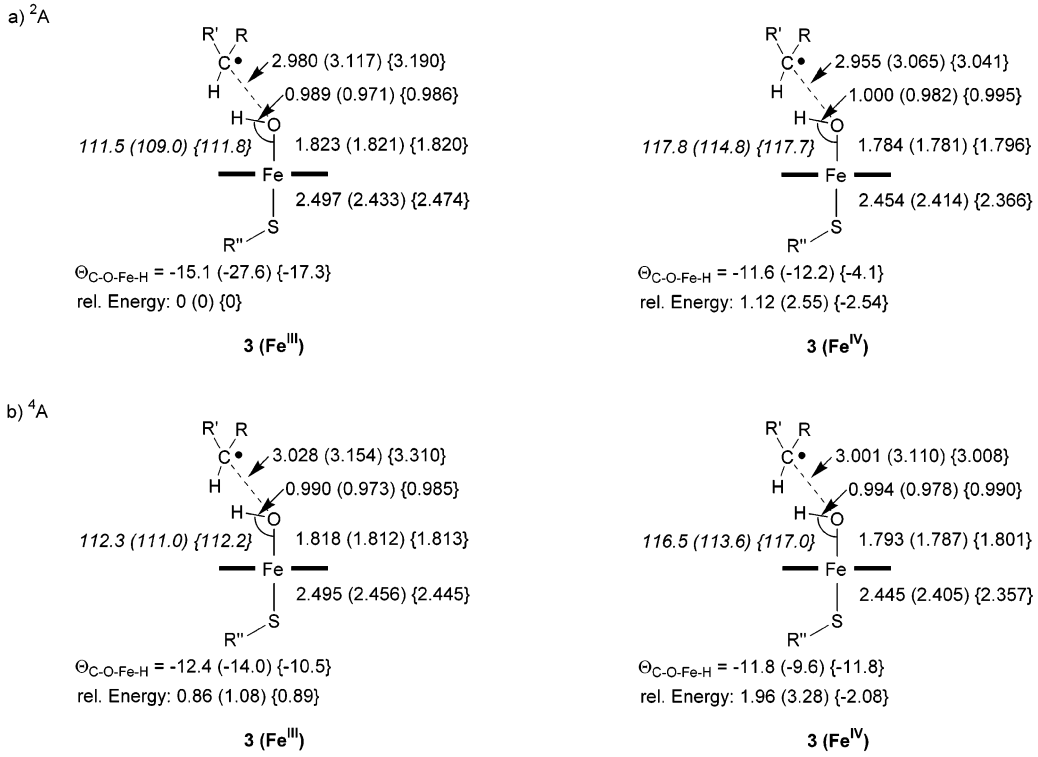

Spin Densities

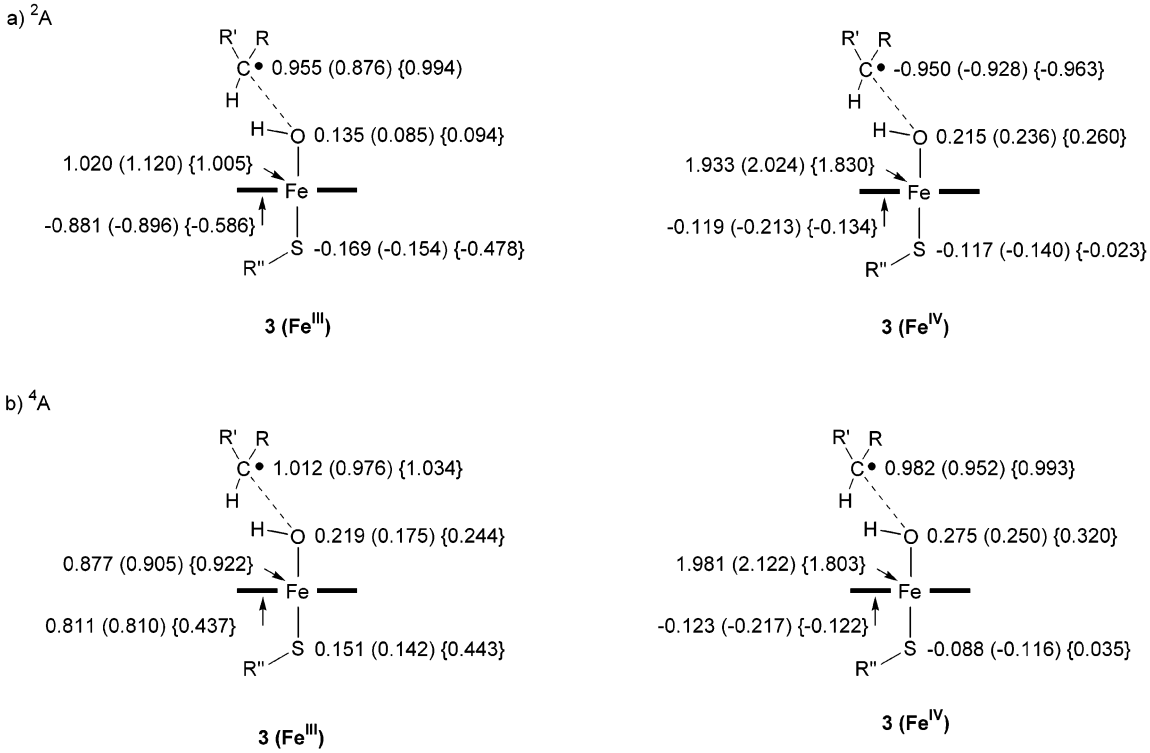

Figure 8. Relative energies (kilocalories per mole), structural data, and spin densities for the intermediate cluster **3**. The labels refer to the following situations: QM/MM optimization of snapshot 40, R1/B1 (QM/MM optimization of snapshot 40, R2/B2) {optimization of the isolated QM system in the gas phase, R1/B1}. Distances are given in angstroms; angles (in italic type) are given in degrees.

labeled ^{2}A-Fe^{III}, ^{2}A-Fe^{IV}, ^{4}A-Fe^{III}, and ^{4}A-Fe^{IV} in the following, specifying the total spin of the complex and oxidation state of the iron atom. Although the energetically lowest ^{4}A and ^{2}A species are of the Fe^{III} variety in the enzyme environment, we also investigated the rebound pathways involving the Fe^{IV}-type systems. The two different electromers (Fe^{III}/ Fe^{IV}) eventually both collapse to the same product **4**, which contains Fe^{III} and a closed-shell porphyrin π system. The rebound process, however, exhibits different barriers, depending on which spin state and electromer is considered.

The energy profile resulting from the one-dimensional scan along $r(C^5-O)$ on the ^{4}A-Fe^{III} surface is shown in Figure S-3 of the Supporting Information. The point with the highest energy occurs at $r(C^5-O) = 2.442$ Å and $\theta(C^5-Fe-O-H^{(5-exo)}) = -60.8°$ and is 9 kcal/mol above **3** (^{4}A-Fe^{III}). Beyond that point the energy drops sharply, and free minimizations starting from such conformations yield the product complex **4**. Starting a transition-state search from the highest energy point of the scan, we located a transition structure (**TS$_{Reb}$**),[54] which was fully optimized by use of QM region R1 and basis set B1. In contrast, the PES for rebound of the other three electronic configurations—i.e., ^{2}A-Fe^{III}, ^{2}A-Fe^{IV}, and ^{4}A-Fe^{IV}—is very flat, such that one-dimensional scans are apparently not sufficient to describe this process. For instance, the one-dimensional energy profile with respect to $r(C^5-O)$ on the ^{2}A-Fe^{III} surface is shown also in Figure S-3. The QM/MM energy slightly increases until the two fragments have approached each other to a distance of $r(C^5-O) = 2.67$ Å. Beyond this point the hydroxyl group flips around the Fe−O axis and the two fragments collapse to give the alcohol complex **4**. The highest QM/MM energy obtained from the scan corresponds to a barrier of 1.7 kcal/mol with respect to the hydroxo intermediate (^{2}A-Fe^{III}). We have performed frequency calculations and transition-state searches starting from this conformation. However, the vibrational analysis gave no mode with an imaginary frequency and the transition-state searches failed to locate a stationary point.

Two-dimensional scans for ^{2}A-Fe^{III}, ^{2}A-Fe^{IV}, and ^{4}A-Fe^{IV} were performed by varying the dihedral angle $\theta(C^5-Fe-O-H^{(5-exo)})$ from 10° to 80° in steps of 10° at $r(C^5-O) = 3.007$, 2.818, 2.755, and 2.696 Å. Figure S-4 (Supporting Information) shows the resulting QM/MM energy profiles as a function of $\theta(C^5-Fe-O-H^{(5-exo)})$ at $r(C^5-O) = 2.818$ Å. At this distance, we obtained the smallest barriers in all electronic states. There are, however, only small variations in the potential energy associated with changes in the range $30° < \theta(C^5-Fe-O-H^{(5-exo)}) < 60°$ for all distances. The PES for rebound is very flat, resembling a flat ridge that separates the intermediate hydroxo cluster **3** from the product complex **4**. The two-dimensional energy profiles are documented in the Supporting Information. Transition-state searches failed to precisely locate the transition structures on the flat PES of the rebound step in these states, and we therefore estimate corresponding activation energies from the points obtained in the two-dimensional scans. This leads to barriers of 0.21 (^{2}A-Fe^{III}), 2.65 (^{2}A-Fe^{IV}), and 2.98 (^{4}A-Fe^{IV}) kcal/mol with respect to the lowest hydroxo complex **3** (^{2}A-Fe^{III}). Unconstrained geometry optimizations starting from the points obtained in the scans confirm that these structures interconnect the hydroxo intermediate **3** and the product **4**. Their relative energies are lower than those of the transition state for hydrogen abstraction: with respect to the reactive complex **2** they are 14.3 (^{2}A-Fe^{III}), 16.7 (^{2}A-Fe^{IV}), and 17.0 (^{4}A-Fe^{IV}) kcal/mol, while **TS$_H$** is calculated at 19.5 (^{2}A) and 20.6 (^{4}A) kcal/mol. This means that the first step in the hydroxylation reaction is rate-limiting, in both the ^{2}A and ^{4}A states. In contrast, the transition structure **TS$_{Reb}$** obtained for the ^{4}A-Fe^{III} configuration has a relative energy of 10.7 (24.8) kcal/mol with respect to **3**, ^{2}A-Fe^{III} (**2**, ^{2}A) and hence is the point of maximum energy in the overall energy profile. It will therefore be irrelevant mechanistically because the quartet path via ^{4}A-Fe^{IV} requires much less activation (see above), unless of course the transformation from ^{4}A-Fe^{III} to ^{4}A-Fe^{IV} is extremely slow. The doublet species may undergo rebound via both states, ^{2}A-Fe^{III} and ^{2}A-Fe^{IV}, with a negligible barrier for ^{2}A-Fe^{III}. Figure 9 gives selected geometric features and spin densities of the structures corresponding to the rebound barriers discussed above.

Turning to the gas phase, a potential energy scan at the B3LYP level (QM region R1, basis set B1) was carried out for the ^{4}A state along the distance $r(C^5-O)$ in the range from 3.7 to 1.2 Å. In contrast to previous gas-phase studies,[11b,15f] the resulting energy profile for the ^{4}A state does not indicate a barrier in the range $2.2 \text{ Å} < r(C^5-O) < 2.6$ Å. Instead, consecutive transition-state searches located a saddle point at $r(C^5-O) = 2.86$ Å, with a low imaginary frequency ($40i$ cm^{-1}), indicative of a very flat potential energy surface at this point. This transition state is 3.72 kcal/mol above the Fe^{IV} hydroxo intermediate **3** discussed above. By further increasing the distance $r(C^5-O)$, we arrived at another conformation of the hydroxo species, which is only 1.68 kcal/mol below the transition state, with a dihedral angle $\theta(C^5-Fe-O-H^{(5-exo)})$ of nearly 180°. Similar observations have been made in previous gas-phase model calculations with methane as substrate for hydroxylation:[11b] the transition state for rebound found in this study does not directly link the product with the energetically lowest hydroxo intermediate but with an energetically less favorable conformation ("rebound cluster"), in which the dihedral angle $\theta(C^5-Fe-O-H^{(5-exo)})$ is 180°. It should be noted that the transition mode for the rebound step in the gas phase is thus characterized by a direct approach along the coordinate $r(C^5-O)$, with the substrate being unhindered and able to rotate freely to attack the oxygen at the free site. In contrast, the QM/MM calculations reveal that substrate motion in the protein pocket is hindered (e.g., by a hydrogen bond from the camphor carbonyl oxygen to Tyr96), and the transition mode involves also rotation of the OH group around the Fe−O axis. Importantly, the electronic structure in the gas phase corresponds to an Fe^{IV} species, as can be seen from the spin densities in Figure 9. No low-lying Fe^{III} transition species was found in the gas phase, as opposed to the situation in the protein environment. Potential energy scans in the gas phase show that the rebound process on the ^{2}A surface is virtually barrierless and therefore cannot be linked to a single transition structure. These findings are consistent with previous gas-phase results; thus, DFT calculations on propene oxidation revealed[55] that the lowest rebound process occurs via the Fe^{IV} electromer, while the Fe^{III} counterpart is significantly higher in energy.

(54) The transition mode with a small imaginary frequency of $92i$ cm^{-1} corresponds to a coupled motion of the O atom approaching C^5, a pyramidalization at the carbon radical center C^5, and a rotation of the OH group around the Fe−O axis.

(55) de Visser, S. P.; Ogliaro, F.; Sharma, P. K.; Shaik, S. *J. Am. Chem. Soc.* **2002**, *124*, 11809.

Geometries and relative energies

a) ^{2}A

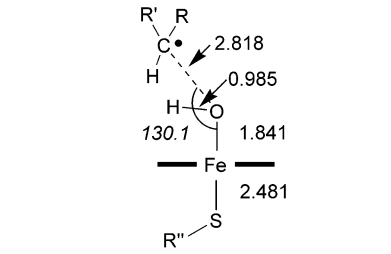

$\Theta_{C\text{-}O\text{-}Fe\text{-}H}$ = -30

rel. Energy: 14.25 (**2**, ^{2}A) / 0.21 (**4**, ^{2}A-Fe^{III})

TS$_{Reb}$ (Fe^{III})

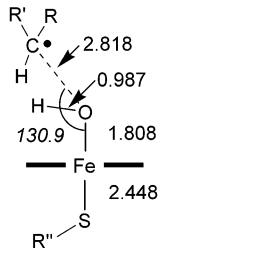

$\Theta_{C\text{-}O\text{-}Fe\text{-}H}$ = -50

rel. Energy: 16.70 (**2**, ^{2}A) / 2.65 (**4**, ^{2}A-Fe^{III})

TS$_{Reb}$ (Fe^{IV})

b) ^{4}A

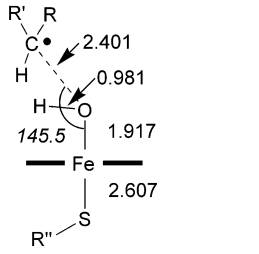

$\Theta_{C\text{-}O\text{-}Fe\text{-}H}$ = -103.3

rel. Energy: 24.75 (**2**, ^{4}A) / 10.71 (**4**, ^{4}A-Fe^{III})

TS$_{Reb}$ (Fe^{III})

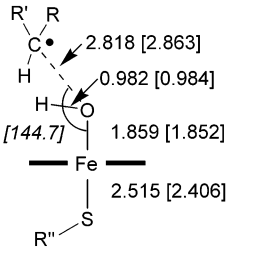

$\Theta_{C\text{-}O\text{-}Fe\text{-}H}$ = -60 [-171]

rel. Energy: 17.02 (**2**, ^{2}A) / 2.98 (**4**, ^{4}A-Fe^{III})
[16.21 (**2**, ^{4}A) / 4.18 (**4**, ^{4}A-Fe^{IV})]

TS$_{Reb}$ (Fe^{IV})

Spin densities

a) ^{2}A

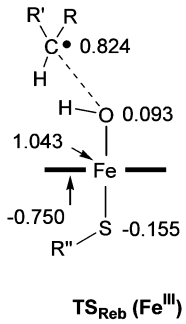

TS$_{Reb}$ (Fe^{III})

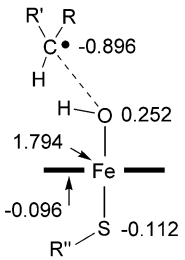

TS$_{Reb}$ (Fe^{IV})

b) ^{4}A

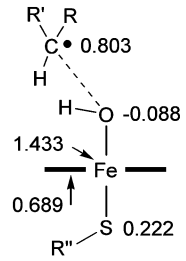

TS$_{Reb}$ (Fe^{III})

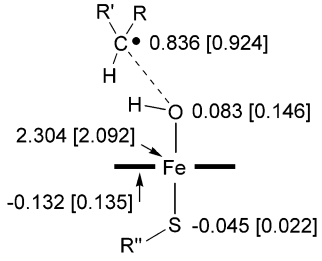

TS$_{Reb}$ (Fe^{IV})

Figure 9. Relative energies (kilocalories per mole) with respect to the species in parentheses, selected structural data, and spin densities for the transition species for rebound (**TS$_{Reb}$**). The labels refer to the following situations: QM/MM optimization of snapshot 40, R1/B1 [optimization of the isolated QM system in the gas phase, R1/ B1]. Distances are given in angstroms; angles (in italic type) are given in degrees.

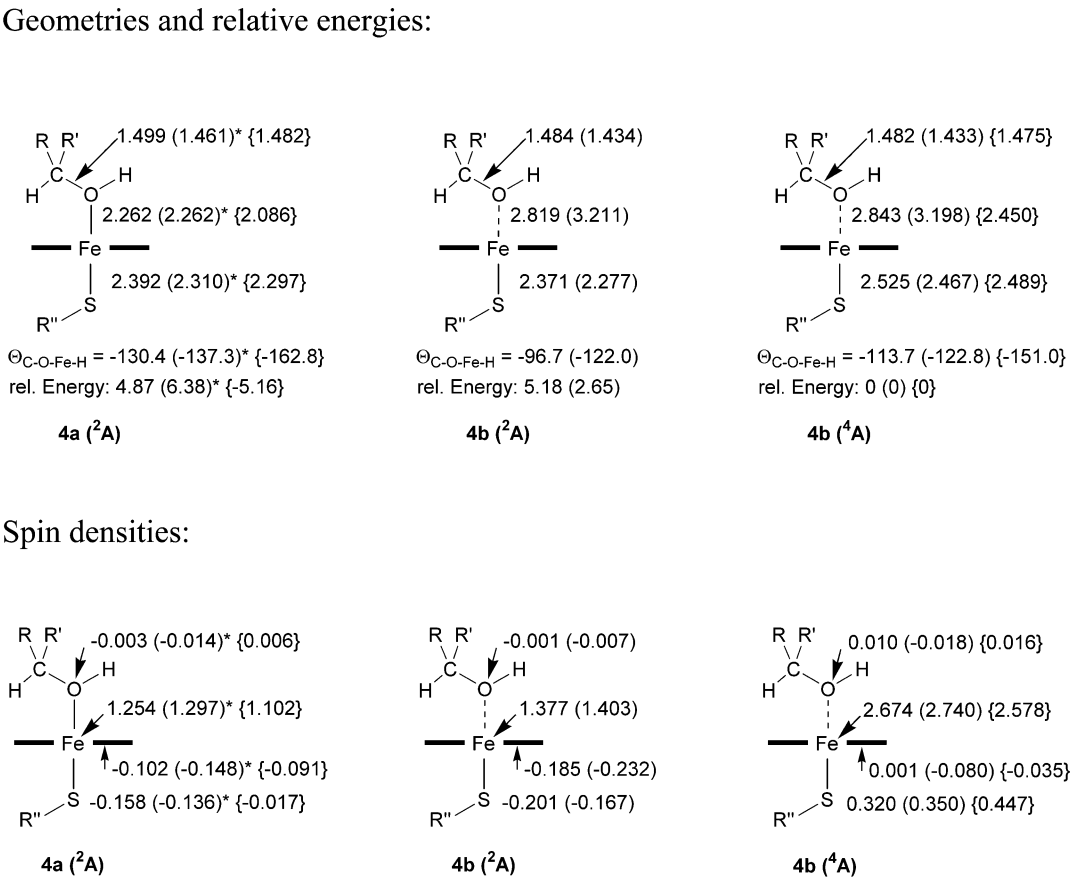

Figure 10. Relative energies (kilocalories per mole), selected structural data, and spin densities for the product complex **4**. The labels refer to the following situations: QM/MM optimization of snapshot 40, R1/B1 (QM/MM optimization of snapshot 40, R2/B2) {optimization of the isolated QM system in the gas phase, R1/B1}. Distances are given in angstroms; angles (in italic type) are given in degrees. Asterisks indicate constrained optimization.

6. Product Complex. Free QM/MM geometry optimizations at the R1/B1 level starting from the last steps of the rebound scan lead to the hydroxycamphor complex **4**. On the doublet spin surface, two stable conformations were found: The first structure **4a** has the product alcohol coordinated to the iron atom and exhibits a relatively short Fe−O distance of 2.26 Å (2.48 Å for snapshot 29). The second species **4b** has the hydroxycamphor dissociated from the heme, leaving a pentacoordinated iron, and is characterized by a long Fe−O distance of ca. 2.8 Å (3.1 Å for snapshot 29). In the quartet state, the Fe−O interaction is repulsive, because an unpaired electron occupies a σ^* molecular orbital of the associated bond. Hence, free geometry optimizations for this state gave only the dissociated structure [distance r(Fe−O) = 2.843 Å]. The sextet state (^{6}A), where five unpaired electrons occupy five d orbitals of iron, was calculated to lie significantly above the doublet and quartet states at short distances r(Fe−O), while it is approximately isoenergetic with the ^{2}A state at larger distances r(Fe−O). Since the sextet state is, however, not relevant in the context of the hydroxylation reaction, it will not be considered further at this point. Details of the product release, including the sextet state, will be published elsewhere. The relevant structural data, relative energies, and spin densities of the doublet and quartet species are summarized in Figure 10.

At the R1/B1 level, the dissociated quartet minimum **4b** (^{4}A) has the lowest relative QM/MM energy; it is approximately 5 kcal/mol more stable than the two doublet conformations **4a** and **4b** (^{2}A) that are nearly isoenergetic. Reoptimization of these structures with the larger QM region R2 and basis B2 also predicts the global minimum to be the dissociated quartet species. Comparing these findings to the isolated QM system in the gas phase, we note remarkable differences: In accord with previous DFT model studies,[11b] there is only one doublet minimum (**4a**) in the gas phase. It is calculated to be more stable than the quartet minimum by 5 kcal/mol. Hence, the ordering of spin states is reversed in the gas phase as compared to the situation in the enzyme environment. One explanation for this finding is offered by the geometry data given in Figure 10: For the ^{4}A state, the optimized Fe−O bond is significantly shorter in the gas phase (2.45 Å) than in the protein (2.84 Å). Since the Fe−O interaction is repulsive in the ^{4}A state, short Fe−O distances are more unfavorable for the quartet. Another factor becomes obvious upon inspection of the calculated relative energies of the species in the gas phase at the geometry optimized in the protein environment ($S_{p,g}$): in this situation the ^{2}A and ^{4}A states are approximately isoenergetic, with the ^{2}A state 0.57 kcal/mol below the ^{4}A state. Hence, the polarization of the electron density in the QM region by the protein environment leads to a stabilization of the ^{4}A state by as much as 5.5 kcal/mol. In conclusion, the comparison of QM/MM results for the protein environment and QM calculations in the gas phase shows notable differences in the relative stability of spin states. The dissociated product complex (Fe−O distance larger than 2.8 Å) is found only in the protein environment, where favorable interactions within the pocket stabilize the hydroxycamphor molecule.

IV. Discussion

The present QM/MM investigations on $P450_{cam}$-mediated camphor hydroxylation are consistent with a two-state reactivity hydrogen abstraction−oxygen rebound pathway, proceeding in the doublet and quartet spin states, as has been suggested earlier on the basis of model calculations.[11] Gas-phase computations on the concerted oxygen insertion indicate significantly higher barriers for this process.

The computed barrier for hydrogen abstraction ($\mathbf{TS_H}$) is similar in the doublet and quartet states, but all calculations consistently predict a slightly lower barrier for the doublet state. After this initial step, the energy profiles bifurcate. On the ^{2}A surface, the rebound step is predicted to proceed with a negligible barrier (0.2 kcal/mol, via ^{2}A-Fe^{III}), whereas the ^{4}A process exhibits a barrier of 2.1 kcal/mol (starting with **3**, ^{4}A-Fe^{III}, and passing through $\mathbf{TS_{Reb}}$, ^{4}A-Fe^{IV}).

In a recent DFT study on camphor hydroxylation in the gas phase, the rebound transition state for the ^{2}A rebound process was found to have a barrier of 0.7 kcal/mol.[15f] This small activation energy has been attributed to the rotational barrier of the camphor molecule to a conformation that is best suited for the rebound reaction. The steric constraints in the protein pocket prevent such a rotation of the substrate in the present QM/MM calculations. Instead, the OH group of the iron−hydroxo complex has to rotate around the Fe−O axis, such that the C−O interaction becomes possible. As discussed previously,[11b,f] a TSR scenario, as met in the present case, is capable of explaining the results of radical clock experiments.[9] These measurements seem to exclude the presence of a discrete radical intermediate and have been interpreted in terms of a nonsynchronous concerted oxygen insertion pathway and a cationic "OH^+ insertion", mediated by iron hydroperoxo complex **1**.[12] In a TSR scenario, the apparent lifetimes[11b] of radical intermediates depend on (i) the relative yield of the ^{2}A and ^{4}A reactions, which is determined by the relative barrier for hydrogen abstraction ($\mathbf{TS_H}$) for these states, and (ii) the relative barriers in the ^{2}A and ^{4}A states for the rebound step. The real lifetime of the intermediate radicals will be longer than the apparent lifetime, if the ^{2}A reaction has lower barriers in both steps. The present QM/MM calculations predict that the bond activation barrier ($\mathbf{TS_H}$) is slightly lower in the ^{2}A than in the ^{4}A state. An even larger preference for the doublet reaction was found in DFT studies on allylic hydroxylation when the effects of the protein electric field and hydrogen bonding were taken into account.[24,55] As a consequence, the measured, apparent radical lifetimes will be unrealistically short compared with the real lifetimes. A recent QM study of one of the Newcomb probe substrates shows TSR[11g] with precisely the same characteristics as here. The doublet reaction is effectively concerted, while the quartet reaction is stepwise, and the respective radical has a rebound barrier that is larger than the barrier for skeletal rearrangement. Therefore, virtually all the rearranged product will be formed from the quartet pathway. Since the doublet pathway has also a lower barrier for H-abstraction, the amount of radical rearrangement will be very small, thereby leading to an ultrashort apparent lifetime for the radical. Likewise, future QM/MM investigations will have to deal with the radical clock systems themselves, to model the actual experimental situation.

In contrast to the present results, recent DFT studies in the gas phase with CH_3S^- as a model of the proximal ligand and camphor as the substrate[15f] predict the barrier for H-abstraction to be lower in the ^{4}A state than in the ^{2}A state. The present gas-phase study of the hydroxylation reaction, with full camphor as substrate and HS^- to represent the sulfur ligand, predicts the barrier in the ^{2}A state to be lower than in the ^{4}A state, like all the QM/MM models (see Supporting Information). It thus seems that the CH_3S^- ligand misrepresents the situation in the enzyme environment. This finding, much the same as the wrong assignment of a $^2\Pi$ (sulfur radical) ground state for compound I,[56,57] is probably due to the strong electron-donor property of this ligand.

The QM/MM barriers for hydrogen abstraction calculated in the present study are 20−22 kcal/mol (see Figure 3), depending on QM region and basis set. R1/B1 calculations of the isolated QM system in the gas phase yield activation energies of 20 kcal/mol. These values are quite close to the activation energies reported in previous DFT studies in the gas phase for different compound I models and similar substrates R (^{2}A/^{4}A: for R = CH_4, 27/27 kcal/mol;[11b] for R = C_2H_6, 16/19 kcal/mol;[15d] for R = camphor, 20/18 kcal/mol[15f]). In agreement with a previous study on methane hydroxylation,[11b] we find that inclusion of ZPE reduces the barrier by ca. 4 kcal/ mol. This effect is mainly due to the loss of the C−H vibrational energy of the bond that is cleaved in the $\mathbf{TS_H}$ species. Quantum mechanical tunneling may be expected to further reduce the effective H-transfer barrier by about 0−3 kcal/mol.[58] It is not yet clear whether tunneling plays a role in H-abstraction in P450 catalysis. For $P450_{cam}$, Sligar and co-workers have estimated intrinsic kinetic isotope effects (KIEs) of 4−5.[6,8] However, in microsomal P450 enzymes, KIEs as high as 11 have been found (norbornane hydroxylation by $P450_{LM-2}$;[59] benzylic hydroxylation of [1,1-d_2]-1,3-diphenylpropane[7]), which are indicative of tunneling. Taking into account all these effects and the intrinsic accuracy of the DFT approach (see Table 1, dependence of computed barriers on chosen density functional), the effective barriers for hydrogen abstraction may be estimated to be 13 (±5) kcal/mol. This value seems reasonable regarding the experimental findings of Davydov et al.,[4] who could not detect compound I in the presence of substrate even at temperatures below 200 K.

Since the calculated barriers are not significantly changed in the gas phase as compared to the enzyme, one might wonder what role the protein environment plays in the present enzymatic reaction. One feature discussed in previous theoretical studies in the gas phase is a significant entropic contribution to the free energy barrier of H-abstraction, which accounts for an increase of ca. 10 kcal/mol in the case of methane hydroxylation,[11b] due to the loss of translational and rotational degrees of freedom of the substrate in the transition state. In enzyme catalysis, this entropic penalty is absorbed into the preceding step of substrate binding (driven mainly by expulsion of water molecules from the binding pocket). Hence, the protein environment effectively lowers the free energy barrier for H-abstraction. A clear indication for this effect is the stable conformation representing the reactive complex, where the substrate and

(56) (a) Green, M. T. *J. Am. Chem. Soc.* **1999**, *121*, 7939−7940. (b) Green, M. T. *J. Am. Chem. Soc.* **2000**, *122*, 9495.
(57) Ohta, T.; Matsuura, K.; Yoshizawa, K.; Morishima, I. *J. Inorg. Biochem.* **2000**, *82*, 141.
(58) Truhlar, D. G.; Gao, J.; Alhambra, C.; Garcia-Viloca, M.; Corchado, J.; Sanchez, M. L.; Villa, J. *Acc. Chem. Res.* **2002**, *35*, 341.
(59) Groves, J. T.; McClusky, G. A.; White, R. E.; Coon, M. J. *Biochem. Biophys. Res. Commun.* **1978**, *81*, 154.

compound I are preorganized in the pocket at a geometry with a linear arrangement C−H−O, which is ideally suited for H-abstraction.

Apart from lowering the entropic cost for H-activation, a second important role of the protein environment in the overall reaction is to control the access of water to the active site. It is known that uncoupling of reducing equivalents is enhanced if water has uncontrolled access to the pocket, if the substrate spends much of its time in the active site at unproductive distances or orientations, or if the substrate is difficult to oxidize.[2,8] The third (and most intriguing) effect of the enzyme environment is the high regio- and stereoselectivity of substrate hydroxylation, which is probably due to selective constraints and preferences of certain modes of substrate movement within the active site.

The hydroxo intermediate **3** exhibits several low-lying electronic states, the lowest of which are ^{2}A-Fe^{III}, ^{2}A-Fe^{IV}, ^{4}A-Fe^{III}, and ^{4}A-Fe^{IV}. The present study demonstrates that the Fe^{III} variety is stabilized by electronic polarization and represents the ground state in the enzyme environment, while the isolated gas-phase species are of the Fe^{IV} type. All these states may be involved in the rebound reaction. The consequences of such a multistate scenario in terms of the kinetics of the reaction will be a subject of future investigations. The rebound barrier is larger in the ^{4}A than in the ^{2}A state; the lowest barriers in the respective spin states are found for the ^{2}A-Fe^{III} (ca. 0.2 kcal/mol) and ^{4}A-Fe^{IV} species (ca. 3 kcal/mol). Another factor revealed by the QM/MM investigations is that the rebound process in the enzyme mainly occurs by OH rotation around the Fe−O bond. Similar observations were made in a QM/MM study on the methane monooxygenase enzyme.[60] This is in contrast to model studies in the gas phase, where the transition mode is characterized by rotation of the alkyl group about the Fe−O bond.[11b,15d,f,55] Clearly, this finding is a manifestation of the selective constraints of the protein pocket with respect to substrate motion. Interestingly, experimental results show that both *exo*- and *endo*-hydrogens are abstracted in camphor hydroxylation, but only the exo product is formed.[8] Hence, the directional effect of the pocket in the rebound step is crucial for the observed stereoselectivity.

Upon comparison of the QM/MM results on the product complex with corresponding gas-phase calculations, it becomes obvious that (i) electronic effects exerted by the protein environment modulate the stability of spin states, thereby favoring the quartet configuration, and (ii) there is a stable conformation of the dissociated doublet product complex in the protein environment, due to favorable interactions of the hydroxylated product with residues in the pocket, which are enhanced in the dissociated product complex (e.g., the H-bond between the camphor carbonyl oxygen and Tyr96). Therefore, the protein environment facilitates the dissociation of the hydroxycamphor molecule from the iron. As a caveat, we stress that the relative energies of spin states in **4** are largely affected by the choice of the density functional. This is due to the admixture of exact exchange, which is known to favor high-spin configurations.[61] Thus, calculations with the BLYP functional (without exact exchange) indeed show that the relative state energies in **4** are changed by several kilocalories per mole with regard to the B3LYP results, leading to a preference for the ^{2}A state. Hence, definite conclusions regarding the multiplicity of the ground state of **4** may be hard to reach at the DFT level. This issue will be addressed in detail elsewhere.

In the recent QM/MM study of Guallar et al.,[26] the authors suggest a mechanism of electrostatic TS stabilization in the H-abstraction step; this is based on their result that the reactant species (**2**) carries significant spin density on the oxygen atoms of the A-propionate side chain of the heme. In the TS for H-abstraction, they find a shift of electron density toward this group, increasing (decreasing) the charge (spin density) on the carboxylate oxygen, thereby intensifying the electrostatic attraction within the corresponding salt bridge to Arg299. This would lead to a stabilization of the TS, effectively lowering the barrier for H-abstraction. Our calculations disagree with these findings, in that they do not predict spin density on the propionate oxygen atoms, if these atoms are screened by surrounding charges, as is the case in the QM/MM study. Through additional QM/MM calculations, we explored some parameters that are different in the two studies and could give rise to the discrepancies: (i) the treatment of protonation state and solvation, (ii) the use of different self-consistent field equations (restricted open-shell vs unrestricted treatments), and (iii) the effect of screening atomic charges on Arg299 (forming the salt bridge with the A-propionate). With regard to point i, our model contains 5652 additional water molecules. Titratable groups of the protein were protonated according to Lounnas and Wade,[62] who assigned protons on the basis of Poisson−Boltzmann calculations. Charged surface residues were not neutralized, since they are screened by the surrounding water (net charge −10e). Imitating the model employed by Guallar et al., we did single-point calculations on QM region R2-S1 in the ^{4}A state, without the bulk solvent, and neutralized surface residues (net charge 0). This led to an activation energy of 24.6 kcal/mol and minor variations in spin densities with regard to the solvent environment employed in our previously discussed calculations, but there is specifically no spin density on the propionate oxygens. With regard to point ii, we solved the Kohn−Sham equations for **2** (QM region R2-S1, snapshot 29) using the restricted open-shell procedure as implemented in Gaussian98.[63] The resulting spin densities were found to be quite similar to those obtained with the unrestricted formalism employed in the present study [ROB3LYP/UB3LYP: ρ(O) = 0.83/0.92; ρ(Fe) = 1.14/1.09; ρ(Por) = 0.70/0.66; ρ(S-cysteine) = 0.34/0.32; ρ(A-propionate) = 0.00/0.00; ρ(D-propionate) = 0.00/0.00]. Finally, with regard to point iii, single-point calculations (R2-S1/B2) were done, with the atomic charges on the Arg299 $[(NH)C(NH_2)_2]^+$ group set to zero, to check the influence of these nearby charges on the spin densities of the

(60) Guallar, V.; Gherman, B. F.; Miller, W. H.; Lippard, S. J.; Friesner, R. A. *J. Am. Chem. Soc.* **2002**, *124*, 3377.

(61) (a) Reiher, M.; Salomon, O.; Hess, B. A. *Theor. Chem. Acc.* **2001**, *107*, 48. (b) Salomon, O.; Reiher, M.; Hess, B. A. *J. Chem. Phys.* **2002**, *117*, 4729.

(62) Lounnas, V.; Wade, R. C. *Biochemistry* **1997**, *36*, 5402.

(63) Frisch, M. J.; Trucks, G. W.; Schlegel, H. B.; Scuseria, G. E.; Robb, M. A.; Cheeseman, J. R.; Zakrzewski, V. G.; Montgomery, J. A., Jr.; Stratmann, R. E.; Burant, J. C.; Dapprich, S.; Millam, J. M.; Daniels, A. D.; Kudin, K. N.; Strain, M. C.; Farkas, O.; Tomasi, J.; Barone, V.; Cossi, M.; Cammi, R.; Mennucci, B.; Pomelli, C.; Adamo, C.; Clifford, S.; Ochterski, J.; Petersson, G. A.; Ayala, P. Y.; Cui, Q.; Morokuma, K.; Malick, D. K.; Rabuck, A. D.; Raghavachari, K.; Foresman, J. B.; Cioslowski, J.; Ortiz, J. V.; Baboul, A. G.; Stefanov, B. B.; Liu, G.; Liashenko, A.; Piskorz, P.; Komaromi, I.; Gomperts, R.; Martin, R. L.; Fox, D. J.; Keith, T.; Al-Laham, M. A.; Peng, C. Y.; Nanayakkara, A.; Gonzalez, C.; Challacombe, M.; Gill, P. M. W.; Johnson, B. G.; Chen, W.; Wong, M. W.; Andres, J. L.; Head-Gordon, M.; Replogle, E. S.; Pople, J. A. Gaussian 98, Revision A.7; Gaussian, Inc.: Pittsburgh, PA, 1998.

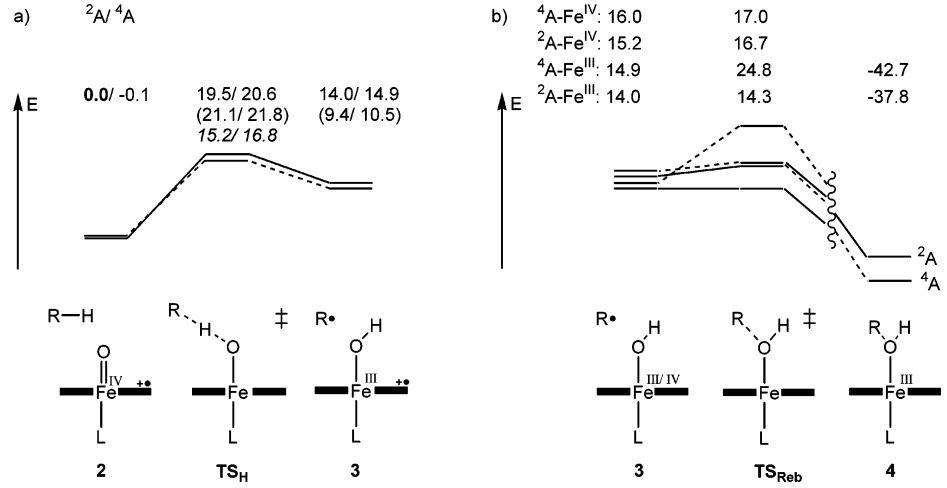

Figure 11. Relative energies (kilocalories per mole): QM/MM optimization of snapshot 40. (a) H-abstraction phase. The labels refer to the following energies: R1/B1, (R2/B2), *R1/B1 including ZPE correction* (note that tunneling corrections may further lower the effective H-abstraction barrier to around 13 kcal/mol). (b) C−O bond formation phase, R1/B1.

A-propionate oxygens. Indeed, the spin density on this group was increased to 0.12e in the reactive complex (**2**) and 0.15e in the transition state for hydrogen abstraction (**TS$_H$**); the barrier is 24.7 kcal/mol. This indicates that the spin densities on the carboxylate oxygens are quite sensitive to a nonoptimal screening, as might, e.g., result from an unfavorable side-chain conformation of Ar299. Although we do not observe an effect on the barrier for H-abstraction by suboptimal screening in the present case, this effect might offer an explanation for the differences in the QM/MM barriers calculated in the two studies.

After the preceding detailed comparisons with experimental and other theoretical work, we close the discussion by summarizing our main results from the QM/MM calculations on snapshot 40 in the form of energy profiles for the hydrogen abstraction and rebound step (see Figure 11). Hydrogen abstraction from camphor by compound I (Fe^{IV}) can occur both in the doublet and in the quartet state, with a slightly lower barrier in the doublet. The resulting intermediates have Fe^{III}-type ground states in the enzyme, but the Fe^{IV} electromers are only slightly higher in energy (by ca. 1 kcal/mol). The rebound step is almost barrierless for the doublet ground state (^{2}A-Fe^{III}) and requires some activation for the lowest quartet state (ca. 9 kcal/mol via ^{4}A-Fe^{III} and ca. 2 kcal/mol via the ^{4}A-Fe^{IV}-type rebound TS; see ref 64 for a qualitative valence-bond analysis of the difference in barrier heights).

V. Conclusion

On the basis of combined QM/MM calculations, the present study provides a complete picture of the hydrogen-abstraction oxygen-rebound pathway, by which P450$_{cam}$ mediates the selective hydroxylation of C−H bonds. Our calculations show that this reaction is typified by TSR, as has been suggested earlier on the basis of model computations. As such, this mechanism provides a satisfactory explanation for seemingly contradictory experimental findings, which on one hand suggested the presence of radical intermediates but on the other hand yielded unreasonably short lifetimes for these intermediates.

We investigated a potential mechanism of electrostatic transition-state stabilization, that implies the selective stabilization of the transition state for hydrogen abstraction by interactions of the propionate side chains of the heme with neighboring positively charged protein residues. Our results demonstrate that there is no charge transfer to the propionate groups and hence no differential stabilization of the transition state. The results from a QM calibration study show that the height of the barrier for hydrogen abstraction largely depends on the chosen density functional; hence quantitative predictions for this activation energy are currently beyond the scope of DFT methods. However, by estimating the effect of zero-point energies and tunneling, we arrive at barriers that seem reasonable with regard to experiments that could not detect compound I even at low temperatures (200 K). It is suggested that the protein promotes the reaction by absorbing the entropic cost that is required to establish the transition state for hydrogen abstraction (ca. 10 kcal/mol) into the process of substrate binding, which is driven by the expulsion of water molecules from the active site and the desolvation of the hydrophobic substrate.

Our calculations furthermore indicate that substrate motion is hindered in the active site, mainly by a hydrogen bond of the camphor carbonyl oxygen with Tyr96. The rebound transition state that is thought to control the stereoselectivity of camphor hydroxylation involves OH rotation, in contrast to substrate rotation, as was found in previous gas-phase model studies; it involves an Fe^{III} species in the doublet state, while the high-spin (quartet) process is of the Fe^{IV} type. Comparative QM calculations in the gas phase established that the protein environment has an effect on the stability of redox electromers (i.e., Fe^{III} vs Fe^{IV} states, porphyrin cation radical vs sulfur radical states) and the relative energies of different spin states. The quartet state in the product complex is stabilized by the polarizing enzyme environment.

Acknowledgment. This research is sponsored by the Binational German Israeli Foundation (GIF). J.C.S. thanks the Fonds der Chemischen Industrie for a Kekulé scholarship.

Supporting Information Available: Absolute and relative energies, selected optimized structural parameters, and spin densities for the concerted oxygen insertion study; the other

(64) Shaik, S.; Cohen, S.; de Visser, S. P.; Sharma, P. K.; Kumar, D.; Kozuch, S.; Ogliaro, F.; Danovich, D. *Eur. J. Inorg. Chem.* **2004**, 207.

snapshots used in the hydrogen-abstraction oxygen-rebound study; gas-phase optimizations on camphor hydroxylation; QM/MM optimizations including porphyrin and Arg299 (R1-S2) side chains; and TDDFT-calculated excitation energies of the hydroxo intermediate **3** (PDF). This material is available free of charge via the Internet at http://pubs.acs.org.

JA039847W